Surface phonons on the Pt(111) surface: A comparison of He-scattering experiments with lattice-dynamical calculations

V. Bortolani, A. Franchini, and G. Santoro
Dipartimento di Fisica, Università degli Studi di Modena, via Campi 213/A, I-41100 Modena, Italy

J. P. Toennies, Ch. Wöll, and G. Zhang
Max-Planck-Institut für Strömungsforschung, Bunsenstrasse 10, D-3400 Göttingen, Federal Republic of Germany
(Received 18 March 1988; revised manuscript received 27 February 1989)

Angular distributions and surface-phonon dispersion curves have been measured by He-atom scattering for clean Pt between $T=160$ and 373 K and for Pt-H(1×1) at 160 K along the $\langle 110\rangle$ and $\langle 112\rangle$ azimuths. Inelastic-scattering intensities over a wide range of wave vectors are also reported for the clean surface. The results are analyzed with use of the distorted-wave Born approximation for a model potential describing the He-atom–Pt-surface potential. A set of 14 force constants adjusted to the bulk-phonon dispersion data cannot explain the measured time-of-flight spectra and the observed first-layer relaxation. However, by modifying at the surface the nearest-neighbor tangential force constants ($\alpha_1''=1.7\alpha_1^b$, and $\alpha_1'=1.3\alpha_1^b$), the radial force constants ($\beta_1''=0.39\beta_1^b$), and the three-body force constant ($\gamma_1''=0.037\gamma_1^b$)—where the superscripts $\parallel$ and $\perp$ denote forces within the surface plane and between the first and second planes, respectively—a good fit to all the data is achieved. The new surface force constants are discussed in terms of electronic-charge redistribution within the first layer.

I. INTRODUCTION

The platinum surface has been extensively studied by a wide range of surface-science techniques. One important motivation behind these efforts is the widespread use of platinum as an industrial catalyst. Until recently, however, little was known about the surface-phonon dispersion curves that reflect the dynamical behavior of the atoms at the surface of the crystal. This information is of interest not only because it provides the most direct information on the forces between atoms in the surface layer, but also for understanding the inelastic coupling of gas-phase particles with the phonon heat bath, questions directly related to the elementary processes of accommodation, and sticking. In previous studies of surface-phonon dispersion curves, He-atom inelastic scattering had revealed an anomalous mode on the (111) surfaces of all the noble metals, Cu, Ag, and Au.[1–3] This anomaly has been attributed to a longitudinal resonance (LR), which arises because of an unexpected strong softening (30–70 %) of the lateral force constants in the outermost layer of these crystals.[4] The currently favored explanation of the anomaly is that the *sp-d* hybridization in the bulk is strongly reduced at the surface. A related interpretation comes from a recent model which represents the electrons in the lattice by massless pseudocharges, whose positions are shifted inwards at the surface.[5] A change in *sp-d* hybridization and similar anomalies are also expected to occur in transition metals such as Pt because of similarities between the hybridization of the electron orbitals in the transition and noble metals. Recently, three different groups reported He inelastic-scattering studies on the Pt(111) surface, and in all three experiments evidence for the same longitudinal resonance was indeed found.[6–8] In two cases[6,7] the results indicated, in addition, one or two Kohn-type sharp anomalies in the Rayleigh-mode dispersion curves at special values of the phonon wave vector along the $\langle 110\rangle$ $\bar{T}$ direction.

The present paper is a more extensive study concerning the interpretation of these experiments, with special attention paid to the very precise experimental data reported by three of the present authors.[6] We focus on the following three issues raised in the first publication. (1) What is the exact extent of the lateral softening of the force constants in Pt(111)? For this it has been necessary to carry out extensive lattice-dynamical calculations of the surface-phonon dispersion curves, initially based on force constants derived from an extensive fit to the bulk dispersion curves. These surface-phonon dispersion curves are then compared with experiment by fully simulating the expected time-of-flight spectra. To achieve a best-fit agreement, it has been necessary to modify the surface force constants. The most important change leads to a reduction of the nearest-neighbor lateral radial force constant to 39% of the bulk value. (2) Similar experiments are reported here for the first time for Pt(111)+H(1×1) and in Pt(111)+D(1×1). In this case the dispersion curves reveal only a Rayleigh mode, and there is no evidence for the LR anomalous mode. Also, no noticeable differences are found between surfaces with the H- and D-atom overlayers. This suggests that the effect of the H atoms is merely to change the electron bonding in the surface layer. The influence of the mass loading due to H atoms can be entirely neglected because of their small mass compared to that of the Pt atoms. By the same best-fit procedure outlined above, the force constants for this system could be also determined. (3) Finally, we have addressed the question of the origin of the

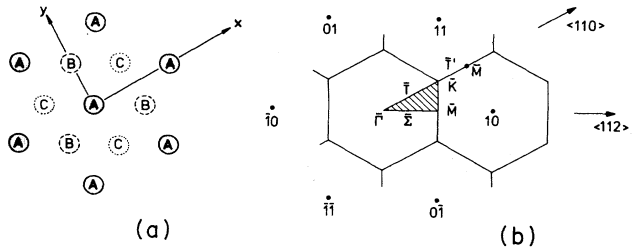

FIG. 1. Schematic diagram showing (a) the positions of the individual atoms in the first three layers A, B, and C of a fcc(111) surface, respectively, and (b) the reciprocal lattice with the first Brillouin zone and the reduced-zone diagram. The real lattice in (a) and the reciprocal lattice in (b) have the same orientations. $\bar{\Sigma}$ and $\bar{T}$ designate the high-symmetry directions in the reduced Brillouin zone. T' is the zone-boundary direction connecting the $\bar{M}$ and $\bar{K}$ points.

sharp anomalies observed in the Rayleigh surface-phonon dispersion curve at special values of the wave vector. By very carefully simulating the Σ_4 bulk dispersion curves along the Γ–K direction so as to include the effect of the Kohn anomalies in the bulk, the calculations mentioned under (1) predict a surface anomaly, which is a projection of the bulk anomaly onto the surface.

Figure 1 shows the stacking in the first three layers of a fcc (111) crystal surface. Also shown is the reciprocal-lattice space, the Brillouin-zone diagram, and the reduced-zone diagram, with the notations that are used throughout this paper. The dispersion curves are measured by adjusting the azimuthal angle to correspond to one of the high-symmetry directions, $\bar{\Sigma}$ or $\bar{T}$, and choosing appropriate incident and final angles. All angles are measured with respect to the surface normal. The velocity distribution of the initially monochromatic beam is measured by a time-of-flight technique and determines the energy of single phonons annihilated ($+\hbar\omega$) or created ($-\hbar\omega$):

$$\frac{\hbar^2}{2m}(k_f^2-k_i^2)=\pm\hbar\omega\ . \tag{1}$$

The corresponding wave vector of the phonon $\mathbf{Q}$ is then determined from conservation of parallel momentum,

$$\mathbf{K}_f-\mathbf{K}_i=\mathbf{Q}\ , \tag{2}$$

where $\mathbf{K}$ is the projection of k onto the surface plane. Only inelastic events in the vicinity of the specular peak were studied, so that the reciprocal-lattice vector $\mathbf{G}=\mathbf{0}$.

The paper begins with a description of the apparatus. Next, the experimental procedures are described. Some typical time-of-flight spectra and the appropriate scan curves showing the kinematical situation are presented together with the determined dispersion curves and the phonon intensities. Section IV describes the theory used to calculate the time-of-flight spectra for comparison with the experiment. In Sec. V the theory is used to analyze the experiments. Section VI discusses the surface force-constant modifications in terms of electron-charge redistribution in the surface layer.

II. APPARATUS

The molecular-beam time-of-flight (TOF) apparatus is much the same as that described earlier[3,9] and is shown in Fig. 2. Essentially it consists of a ^{4}He nozzle-beam source, a target chamber, and a long drift tube followed by an electron-bombardment ionizer and mass spectrometer. Some important features of the apparatus are summarized in Table I.

The highly expanded nozzle beam (nozzle diameter 10 μm) is operated under conditions in which quantum effects lead to a considerable increase in the speed ratio.[10] At a stagnation pressure of 100 bars ($T_0=150$ K), corresponding to $P_0d=1\times10^{-3}$ bar m, the measured speed ratios, after correction for time-of-flight smearing, is $S=170$, in good agreement with theory.[10] The fully expanded beam is chopped by a rotating disk in the next pumping chamber and then passes through two additional differential pumping chambers before striking the target surface. Most of the measurements reported here were carried out with the angle between incident and outgoing beam fixed at $\theta_{SD}=90°$, although other angles between $\theta_{SD}=50°$ and 200° can be chosen. The change in wave vector parallel to the surface, $\Delta K=k_f\sin\theta_f-k_i\sin\theta_i$, is then given by $k_f\cos\theta_i-k_i\sin\theta_i$, where k is the He-atom wave vector and θ is the scattering angle measured with respect to the surface normal; i and f refer to initial (incident) and final states, respectively. The pressure in the scattering chamber is typically 5×10^{-11} mbar with the He beam turned off, and rises to about 4×10^{-9} mbar when the chopped He beam is admitted to the scattering chamber. The scattering chamber is equipped with a cylindrical mirror Auger

TABLE I. Some important features of the He-atom surface scattering apparatus.

Source	
Nozzle diameter	$d=10$ μm
Nozzle stagnation pressure	$P_0=50$–400 bars
Nozzle stagnation temperature	$T_0=40$–450 K
He-beam velocity at $T_0=100$ K	$v_0=\sim1000$ m/sec
Relative velocity spread	$\Delta v/v=\sim1\%$
Source-target geometry	
Distance source to target	43.3 cm
Diameter of beam on target at $\theta_i=45°$	~3 mm
Angular spread of atoms striking target	0.4°
Chopper	
Transmitted pulse FWHM	10 μsec
Chopper frequency	300 Hz
Pulse repetition rate	600 Hz
Target-detector geometry	
Distance from target to center of ionizer	120.2 cm
Angle subtended by detector	0.2°
Estimated effective length of the ionizer	1.5 cm

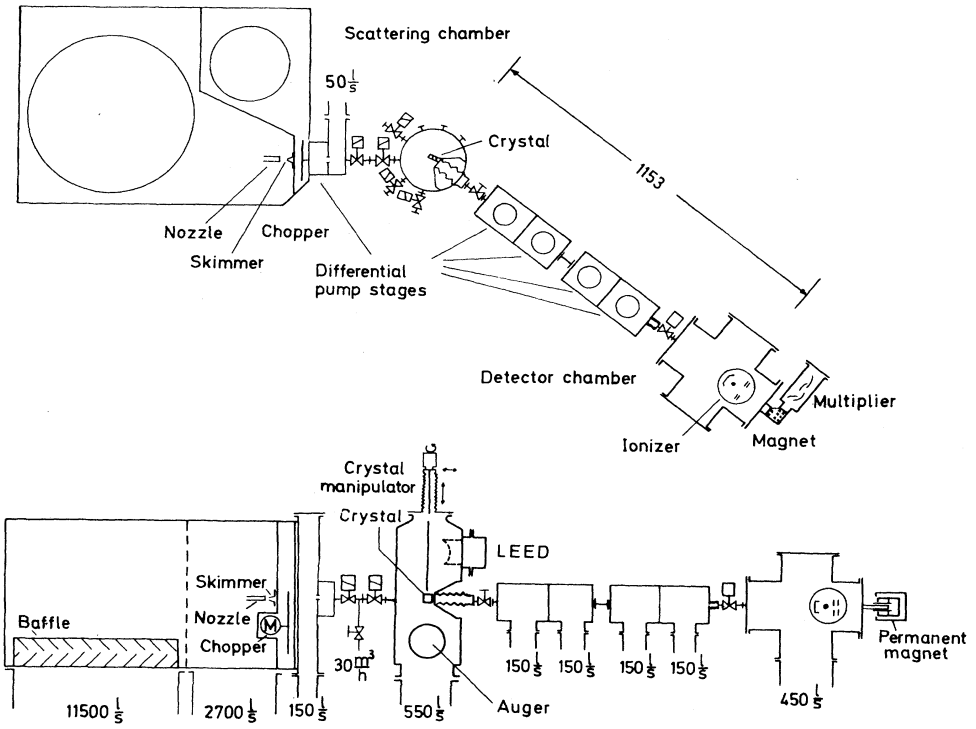

FIG. 2. Schematic top and side view of the surface scattering apparatus used in the present experiments. The beam-source chamber is mounted at the left, the target chamber in the center, and the time-of-flight tube and the mass spectrometer detector on the right. Note the extensive use of differential pumping stages—three between source and target and four between the target and detector chamber. The detector can access all angles θ_{SD} between 50° and 200° measured between the incident and final beams. A coarse adjustment is achieved by rotating the target chamber and attaching the source to the desired entrance port, while the fine adjustment (±20°) is facilitated by the bellows.

analyzer (Physical Electronics model 10-155). The low-energy electron-diffraction (LEED) unit, however, was not in operation during these measurements.

The mass spectrometer employs a homemade open-cage electron-bombardment ionizer with an entrance aperture of 2.3×6.3 mm^2.[11] The ions are mass selected by a permanent-magnet mass spectrometer with 10 cm radius and a pole-shoe spacing of 15 mm, and then strike the first dynode of an open Venetian-blind multiplier [Thorn (EMI) type 9642/3B]. The overall efficiency of the ionizer–mass-spectrometer combination has not been determined absolutely, but is estimated to be about 1 detected ion for 10^5 incident atoms.[12]

The time-of-flight distributions are measured by a CAMAC module (Firma Struck, Hamburg) consisting of a shift register with a variable time channel, which was set typically at 3 μsec during these measurements. The "start" pulse taken from the chopper was delayed so that it is compared directly to the "stop" pulse of the same "bunch" of atoms arriving at the detector. In this way drifts in the chopper frequency cannot affect the flight time. The data are stored and processed in a minicomputer (Digital Equipment Corporation PDP11/23).

The 7-mm-diam crystal boule[13] was first oriented to better than 0.5° using Laue backscattering, and a 2-mm-thick disk was cut off by spark erosion. The disk was polished mechanically down to 1 μm and then chemically etched prior to further treatment in vacuum. After several cycles of prolonged (several hours) neon sputtering (5×10^{-5} mbar, 1 kV, 10 μA/cm^2) followed by annealing to 1000 °C for about 1 h, the main impurities—C, Ca, S, and P—could be removed from the surface. The remaining carbon contamination can be depleted by many repeated sputtering (5×10^{-5} mbar, 500 V, 4μA/cm^2, 15 min) and heating (600 °C for 5 min) cycles. After this procedure the amount of carbon detected in the Auger spectrum was less than 0.5% of a carbon monolayer.

The measuring time of a single time-of-flight spectrum varies over a wide range depending on the Q of the phonon under investigation. For $Q<0.1$ Å^{-1}, it is typically 5 min; for $Q=\frac{1}{2}Q_{BZ}$ (Q_{BZ} is the Brillouin-zone boundary) it is 20 min, while for $Q=Q_{BZ}$ it can be as much as 60 min. The crystal was flashed for 5 min to 600 °C whenever the specular intensity had dropped by a factor 2, typically after 6 h. In this connection it should be remembered that helium scattering is very sensitive to even small amounts of contamination. For example, a coverage of only ~3% of a monolayer of H_2 corresponds to a decrease of specular intensity of ~30%.[14]

An important source of systematic error arises from drifts in the energy of the incident He-atom beam. To reduce these the source temperature was controlled by a

small computer, and the resulting temperature fluctuations were observed to be less than 0.2 K. In all time-of-flight spectra the incident-beam energy was, in fact, determined from the position of the diffuse elastic peak. The absolute incident wave vector was also checked by comparison with the angular locations of the diffraction peaks. Another source of systematic and statistical errors arises from uncertainties in the angular position of the crystal. These were substantially reduced by using only the settings of the computer-controlled stepping motor ($\Delta\theta=0.01°$) to determine relative angular settings. Previously, these had been read off the manipulator with a relative accuracy of only about $\Delta\theta=0.1°$.

III. EXPERIMENTAL RESULTS

A. Clean Pt(111) surfaces

In order to check the alignment of the crystal and the quality of the surface, angular distributions were measured with the unchopped beam. Figure 3 shows the intensity scans measured on one side of the specular peak for both the ⟨112⟩ and ⟨110⟩ directions. The steep dropoff in intensity of 4–5 orders of magnitude with change in surface wave vector indicates that the surface is largely free of defects.[15] Above the smoothly varying incoherent background, weak diffraction peaks are observed in both azimuths. The small size of the peaks is attributed to the very weak corrugation of the densely packed (111) surface. Thus, the first diffraction peaks were seen on the (111) surfaces only as late as 1976 by Boato[16] and Horne and co-workers.[17] As far as we are aware, the present measurements are the first reported experimental results showing a second-order peak in the ⟨112⟩ direction and the first reported experimental results showing diffraction in the ⟨110⟩ direction. As indicated in the insets in Fig. 3, in terms of a billiard-ball model this densely packed direction is expected to have an even smaller corrugation than the ⟨112⟩ direction. The intensities of the diffraction peaks have an estimated

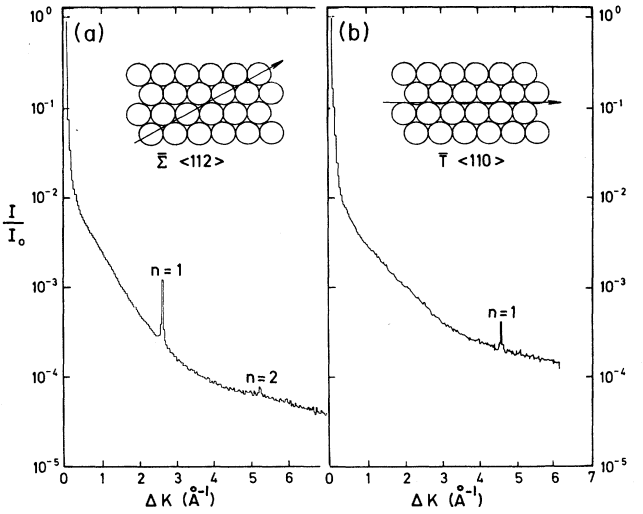

FIG. 3. Angular distributions measured for the Pt(111) surface along the two symmetry directions (a) ⟨112⟩ and (b) ⟨110⟩. The insets show the different geometries of the surface atoms seen when looking down on the crystal surface. Note that the steep dropoff in the intensity with change in surface wave vector indicates a surface which is largely free of defects. The incident wave vector in (a) is $k_i=7.83$ Å^{-1} ($E_i=32$ meV) and $k_i=6.78$ Å^{-1} in (b) ($E_i=24$ meV). The total specular intensity is typically about $I_0=10^7$ counts/sec.

uncertainty of about ±30%. This is attributed to the sharpness of the peaks and the resulting high demands on the precise adjustment of the manipulator, especially with respect to out-of-plane tilt. Nevertheless, to provide a quantitative estimate of the small corrugation we have determined the corrugation amplitude of an equivalent hard corrugated wall potential using the eikonal approximation. The approximate model given by Garibaldi *et al.*[18] has been adapted to the (111) surface geometry. The corrugation function is

$$
\begin{aligned}
z(R)=&2\xi_1^{(2)}\left\{\cos(G_2 y)+\cos\left[G_2\left[\frac{\sqrt{3}}{2}x+\frac{y}{2}\right]\right]+\cos\left[G_2\left[\frac{\sqrt{3}}{2}x-\frac{y}{2}\right]\right]\right\}\\
&+2\xi_2^{(2)}\{\cos(G_2 y)+\cos[G_2(\sqrt{3}x+y)]+\cos[G_2(\sqrt{3}x-y)]\}\\
&+2\xi_1^{(0)}\left\{\cos(G_0 x)+\cos\left[G_0\left[\frac{x}{2}+\frac{\sqrt{3}}{2}y\right]\right]+\cos\left[G_0\left[\frac{x}{2}-\frac{\sqrt{3}}{2}y\right]\right]\right\},
\end{aligned}
\tag{3}
$$

where x and y are orthogonal coordinates in the real space of the surface plane (see Fig. 1) and z is normal to the surface; G_0 is the reciprocal-lattice vector along the ⟨110⟩ direction and G_2 that along the ⟨112⟩ direction. The best-fit results for the corrugation amplitudes $\xi_1^{(2)}$, $\xi_2^{(2)}$, and $\xi_1^{(0)}$ are listed in Table II. Our value of 0.002 Å for $\xi_1^{(2)}$ corresponds most nearly with the corrugation amplitude of 0.01 Å reported by Lee *et al.*[19] The difference can be explained by the much greater beam energy of 107 meV used in their experiments and to a lesser extent by the different model for the hard-wall corrugation.

Quantitative information on the concentration of steps and other defects can also be extracted from the angular distributions. In another study we have reported the effect of a sputtering-induced step concentration on the wide-angle elastic-scattering angular distribution.[15] If the steps are randomly distributed, then the diffraction from the single steps adds up incoherently, leading to a

TABLE II. Corrugation parameters for Pt(111) determined from a best fit of the diffraction intensities with the eikonal approximation.

Direction	E_i (meV)	(2) ξ (Å) 1	(2) ξ (Å) 2	(0) ξ (Å) 1
⟨110⟩	24	0.002±0.001	0.001±0.001	0.001±0.001
⟨112⟩	32	0.002±0.001	0.0004±0.0001	0.0008±0.0001

series of broad undulations in the angular distribution of elastically scattered particles extending out to the largest ΔK values. The fact that this is not observed in Fig. 3 indicates that the step concentration is less than about 1 in 500 Å. This was confirmed by high-resolution measurements of the specular intensity as a function of the incident wave vector over a wide range of collision energies using essentially the same technique described in Ref. 20. Such measurements with He atoms reveal a series of equally spaced maxima and minima corresponding to constructive and destructive interference from adjacent terraces. From the amplitude of these undulations the average concentration of steps can also be determined.[21,22]

For the determination of the surface-phonon dispersion curves, more than 500 time-of-flight spectra were measured. In the data analysis the TOF spectra were transformed from a time-of-flight to an energy-transfer axis using standard procedures, to facilitate the interpretation of the data.[23,24] Figure 4 shows typical time-of-flight spectra converted to an energy-transfer scale for the ⟨112⟩ direction showing both annihilation and creation branches. In order to achieve optimal conditions, the experiments were performed at different values of the beam energy. Since the resolution is best and the multiphonon background is smallest at low collision energies, phonons with small wave vectors were studied using the lowest incident energies of 9 meV ($T_0=50$ K). Near the zone boundary this energy is no longer sufficient for phonon creation and higher energies are necessary, also to assure a sufficient intensity in the creation branch.

The low-energy transfer flanks of the peaks in the spectra of Fig. 4 have been fitted to a Gaussian distribution. The baseline of the Gaussian distribution was chosen so as to correspond to the weak broad maximum underlying most of the spectra and attributed to multiphonon events.

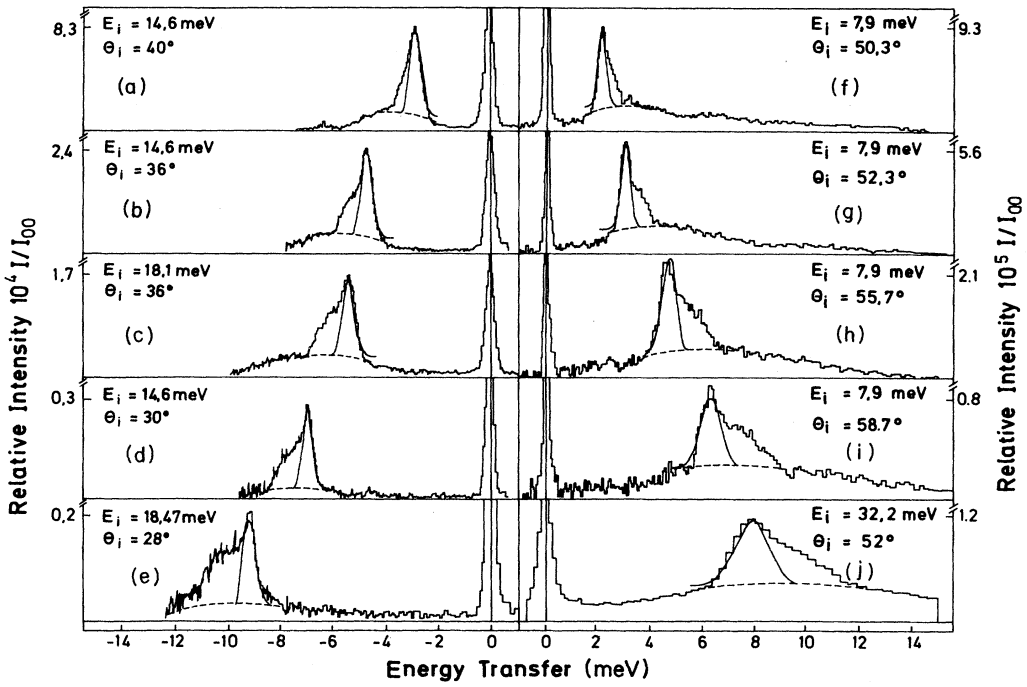

FIG. 4. Typical energy-change histograms obtained from time-of-flight spectra measured at several incident energies E_i on a clean Pt(111) surface along the ⟨112⟩ direction, at various incident angles θ_i for a fixed angle $\theta_{SD}=90°$ between incident and final beams. The wave vector Q corresponding to the inelastic maxima increases from top to bottom. The solid lines are Gaussian distributions for which the peak height and width have been adjusted to fit the spectra. It should be noted that the resolution for creation (left-hand panel) is better than for annihilation (right-hand panel). The crystal temperatures in experiments (a)–(e) was $T_{Pt}=300$ K. For experiments (f)–(j) the temperature was increased to $T_{Pt}=373$ K to enhance the inelastic intensities.

The width of this single peak was found to agree very well with the calculated overall resolution of the apparatus.[24] For this reason we assign this first peak to the Rayleigh mode. The observed width is entirely due to apparatus effects and the intrinsic width of the Rayleigh mode is therefore much smaller. It is seen that the spectra are not adequately fitted by this single mode and that additional modes with larger energy transfer are needed.

In Fig. 4 there are rather large differences in the half-widths of the Rayleigh-mode peak for creation and annihilation which become especially noticeable in comparing the two spectra with the largest energy transfers. This difference can be understood by examining the scan curves and their intersections with the dispersion curves in an extended-zone diagram. The scan curves, it is recalled,[24,25] show the range of observable values of $\hbar\omega$ and Q for a given incident-beam energy and incident and final angles. Figure 5(a) shows the scan curves and dispersion curves corresponding to the time-of-flight spectra of Fig. 4. There it is seen that the angle between the scan curves and the dispersion curves is close to 90° for the backward ($\Delta K<0$) annihilation branch as well as for the forward ($\Delta K>0$) creation branch. Under these conditions the time-of-flight resolution is expected to be greatest. In the other case, in which the scan curve and dispersion curve are parallel, the time-of-flight spectra are completely smeared out over the corresponding region of intersection of the two curves. This purely kinematic effect is called kinematic focusing.[25–27]

Figure 6 shows a series of time-of-flight spectra for phonon creation along the ⟨110⟩ direction. The corresponding scan curves are shown in Fig. 5(b). These spectra appear to be very similar to those along the ⟨112⟩ direction. As in Fig. 4, only the initial rise has been fitted with a Gaussian distribution to provide the location of the Rayleigh mode. However, along this direction the contribution from the bulk bands appears to be more pronounced. For example, as we shall see in Sec. V, the theory explains the structure observed in the spectrum at $\theta_i=41.75°$ between $\Delta E=-4.0$ and -7.5 meV in terms of the density of states of bulk phonons between the transverse and longitudinal thresholds. The intensity beyond -7.5 meV is due to the density of states of the longitudinal bulk bands. In the spectrum taken at $\theta_i=35.75°$, the broad maximum at $\Delta E=-10$ meV corresponds to the lower edge of the longitudinal band. Note that along the ⟨110⟩ direction, in contrast to the

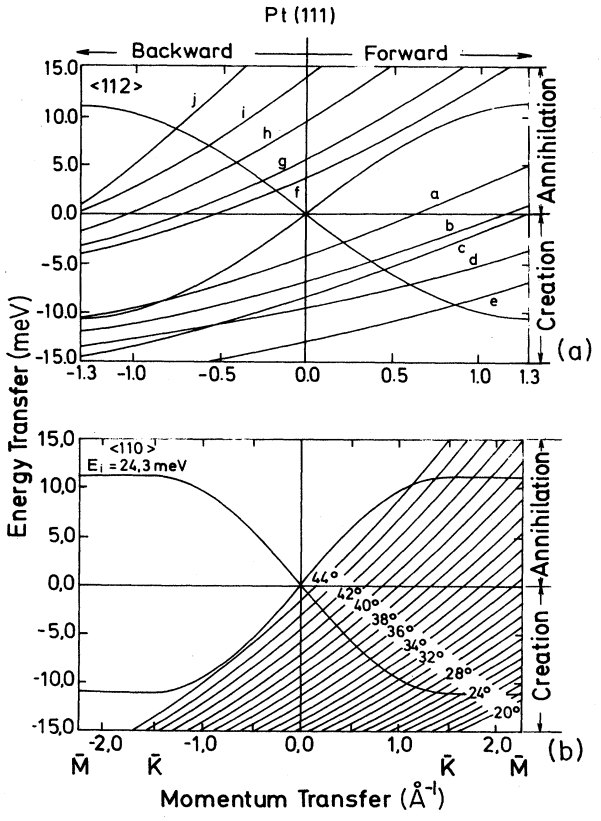

FIG. 5. Scan curves for scattering of He are shown by the parabolas for the conditions of the experimental energy-transfer histograms and compared with the corresponding dispersion curves of the Rayleigh phonons. In (a) the small letters next to the scan denote the corresponding energy-change histograms shown in Fig. 4. In (b) only the scan curves are shown which cross the forward creation branch for a fixed incident energy of $E_i=24.3$ meV, corresponding to the experimental conditions of the spectra in Fig. 6.

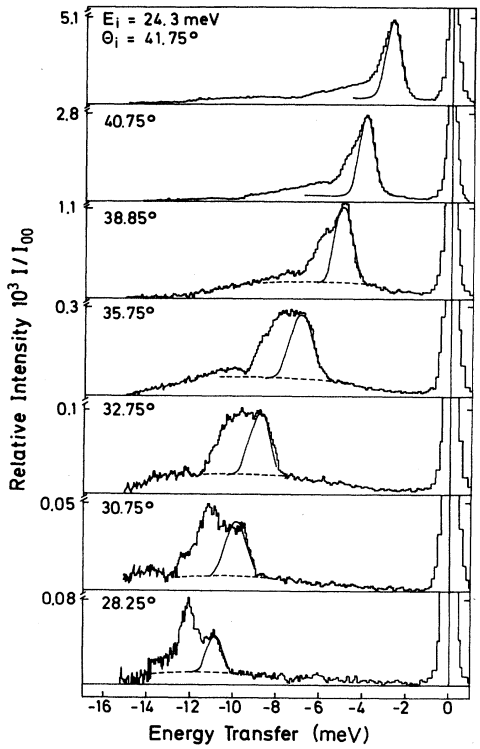

FIG. 6. Typical energy-loss histograms obtained from time-of-flight spectra measured at different incident angles θ_i on a clean Pt(111) surface along the ⟨110⟩ direction, corresponding to creation events for a fixed angle $\theta_{SD}=90°$ between incident and final beams. The solid lines are Gaussian distributions for which both peak height and width have been adjusted to fit the initial rise of the first part of the spectra. Note that a better fit is provided by the theoretical calculations of Sec. IV, which reveal that, in fact, three inelastic maxima are present.

⟨112⟩ direction, the unresolved part not explained by the Rayleigh mode at large energy transfers becomes larger than the first peak. The reason for this difference will become evident from the theory, which reveals that, in fact, three incompletely resolved peaks are contributing to these broad energy-loss distributions.

The Rayleigh mode, whose location is determined by the initial rise of the inelastic structure, was examined more carefully as a function of temperature by carrying out a succession of measurements at 160 and 373 K. The results of both sets of measurements are shown in Fig. 7. First, we note that there is a distinct difference in the dispersion curves at the two temperatures. The observed increase in frequency with increasing temperature is similar to what is observed in the bulk.[28] As far as we are aware, this is the first observation of a temperature effect in surface-phonon dispersion curves. Note also that there is a small hint of a modulation in the otherwise smooth dispersion curve measured at $T=160$ K that is particularly apparent in the region of $0.5 \leq Q \leq 1.2$ Å^{-1}. This structure we previously attributed to Kohn-like anomalies at the surface[6,7] and will be discussed at greater length in Sec. IV. At small Q the points have been fitted to a straight line and its slope is a measure of the sound velocity. The experimental value of 11.1 meV Å is greater than the predicted value of 10.1 meV Å (1531.8 m/sec) calculated from elastic constants for $T=0$ K.[29] Part of the discrepancy may be explained by the difference in temperature between experiment and theory.[30] Note also that the Rayleigh mode is very weak along this direction and probably lies above the transverse bulk band edge (see Sec. V).

Figure 8 shows the intensities of the first peak as a function of the momentum transfer. These intensities were determined by taking the areas under the corresponding Gaussian peaks. The solid lines show the theoretical Rayleigh intensity and will be discussed later. At the zone boundary the intensity is down by about 4 orders of magnitude compared to the specular peak. As compared to data presented previously for the Ag(111) and the Cu(111) surfaces, which show a nearly perfect exponential falloff,[31] the present data appear to show a slight upward curvature, especially beyond $Q=1.0$ Å^{-1}. This curvature is probably related to the relative influence of the attractive and repulsive potentials on the phonon-excitation probability.[31]

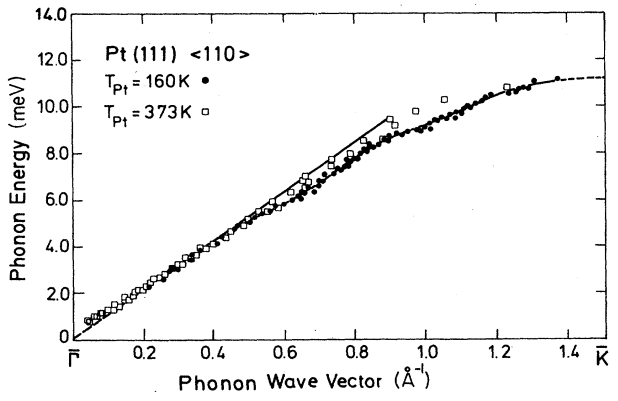

FIG. 7. Measured Rayleigh dispersion curve along the ⟨110⟩ direction for two different surface temperatures $T_{Pt}=160$ and 373 K. The straight line is a best fit of the $T_{Pt}=160$ K data at small wave vectors and has a slope of 11.1 meV Å, corresponding to 1686 m/sec.

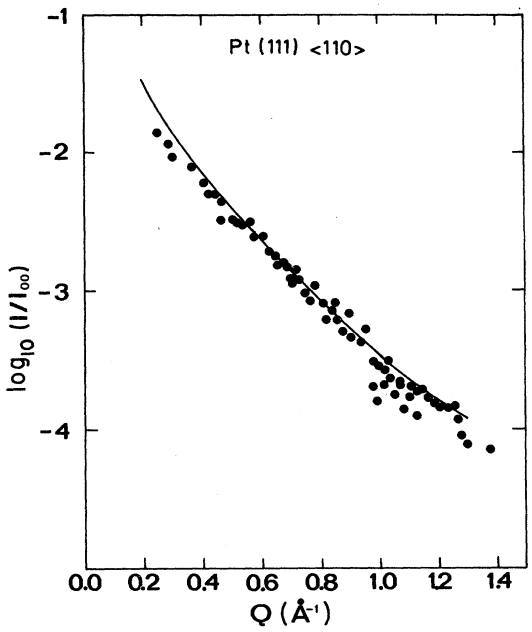

FIG. 8. Experimental intensities of the lowest energy-transfer peak in the time-of-flight spectra measured along the ⟨110⟩ direction compared to the calculated intensities of the Rayleigh mode. The calculations are described in Sec. IV. The target temperature T_{Pt} was 160 K and the incident energy E_i was 24.3 meV.

B. Pt(111)+H(1×1) surface

The effect of H_2 adsorption on the structure of the Pt(111) surface has previously been extensively studied by LEED (Refs. 32 and 33) and by helium-atom scattering.[19] Additional results have recently become available from ion backscattering[34,35] and from calculations based on the linearized augmented-plane-wave method.[36] The LEED and He-atom results indicate a (1×1) structure of the hydrogen overlayer. The early assignment of the H atoms to threefold hcp sites[37] above the surface layer has been disproved by the medium-energy ion-scattering (MEIS) experiments,[34] which indicate fcc sites. Theory predicts that the H atoms lie about 0.95 Å (Ref. 36) above the surface layer of Pt atoms, in reasonable agreement with the experimental value of 0.70±0.2 Å.[34]

Figure 9 shows the results of our measurements of angular distributions along the ⟨112⟩ azimuthal direction obtained after adsorption of 150 L (1 L=1 langmuir=10^{-6} Torr sec) of H_2 at a temperature of 160 K. The adsorption leads to a strong enhancement of the weak clean-surface diffraction peaks, which increase by a factor of about 30. The hard-wall corrugation has been calculated to be $\xi_1^{(2)}=0.025\pm0.005$ at $E_i=24$ meV for the ⟨112⟩ direction. This value is smaller than the value of 0.13 Å reported by Lee *et al.*[19] by a factor of 5, which is

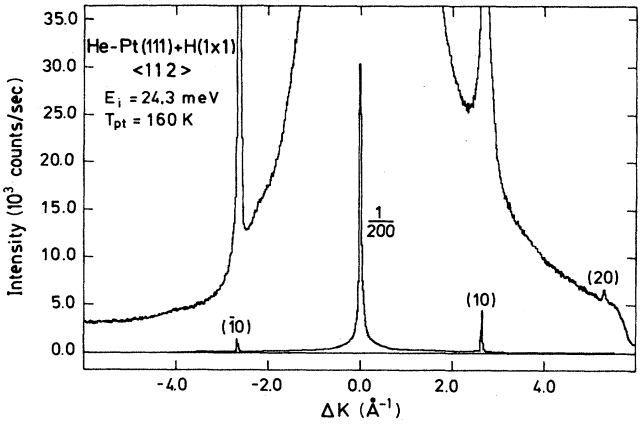

FIG. 9. Angular distributions measured for the Pt(111)+H(1×1) surface after exposure to 150 L of H_2 at $T_{Pt}=160$ K. By comparing with Fig. 3, it is apparent that the corrugation is greatly increased over that for the clean surface. The incident beam wave vector was $k_i=6.8$ Å^{-1} ($E_i=24.3$ meV) and $\theta_{SD}=90°$. The differences in the intensities of the diffraction peaks are attributed to slight misalignment of the tilt angle. [1 langmuir (L)$\equiv 10^{-6}$ Torr sec.]

the same factor found for the difference in corrugation of the clean surface and attributed to the much higher beam energies in the experiments of Lee *et al.*[19] The large increase in corrugation with hydrogenation has already been discussed in the literature by Lee *et al.*,[19] as well as by Batra.[37] It is explained by the linear displacement of the adsorbed H atoms, which are in a plane raised by about 0.95 Å above the plane of the outermost layer of Pt atoms.

Figure 10 shows a series of time-of-flight spectra taken along the ⟨112⟩ and ⟨110⟩ directions for the Pt(111)+H(1×1) surface. The spectra appear quite different from those for the clean surface, since they are better fitted by assuming only one peak, which is attributed to the Rayleigh mode in both directions. As will be discussed in connection with Fig. 20, where the dispersion curve is compared with theory, the Rayleigh mode lies considerably lower than that for the clean surface. At $\bar{K}$ and $\bar{M}$ the experimental frequencies are 9.5 and 9.3 meV, compared to 11.1 and 10.8 meV for the clean surface, respectively. This apparent disappearance of additional modes along the ⟨112⟩ direction and in the ⟨110⟩ direction, and the frequency reduction of the Rayleigh mode, will be discussed in Sec. V.

IV. THEORY

At present, a microscopic theory for the total energies and their derivatives in the noble and transition metals, which is able to account for the *sp-d* electronic hybridization and the presence of the surface, is not available.[38] One noteworthy step forward in this direction is the recent *ab initio* total-energy calculation of Ho and Bohnen for Au(110), which, for the first time, is able to predict the observed relaxation.[39] However, for bulk Pt we note that even for the electronic states only a few *ab initio* studies have been reported.[40] In view of this situation we

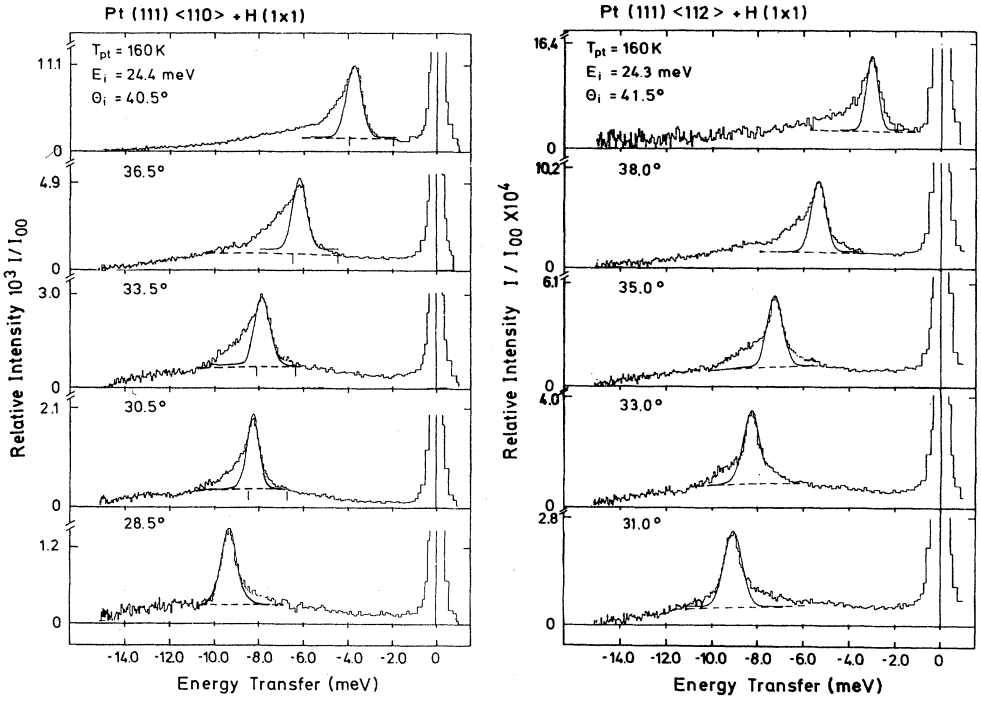

FIG. 10 Some typical energy-loss histograms obtained from time-of-flight spectra measured at different angles on Pt(111)+H(1×1) along the (a) ⟨112⟩ and (b) ⟨110⟩ directions. In both cases for reasons of resolution the incident angles were chosen to observe creation events ($\theta_{SD}=90°$). The solid curves are best-fit Gaussian distributions. Note that there is no evidence for more than one inelastic peak in most of the spectra.

must fall back on a more qualitative description of bonding in the transition metals. In this picture the interaction between the *d* shells is regarded to be repulsive, while the *sp* electrons provide for an attractive force. The *sp-d* hybridization can be looked upon as giving rise to a strong three-body interaction that produces a depletion of charge in some regions around the atoms and a sharp increase in directed bonding charge at the midpoints between first-nearest neighbors. In many respects this bonding is similar to that in the semiconductors.[41] The presence of the surface is expected to strongly affect the distribution of electrons near the surface, so that the bonding charge and also the charges around the atoms are considerably different from those of the bulk. This was first pointed out by Smoluchowski,[42] and later discussed by Finnis and Heine[43] and by Marks and Heine.[44] Since for the nearly-free-electron metals, the three-body forces are relatively weaker, we do not think that the *ab initio* calculations performed for the simple-metal surface Na(100) by Beatrice and Calandra[45] and for Al(110) by Ho and Bohnen[46] and by Eguiluz *et al.*[47] can reproduce the real situation occurring in noble and transition metals. To account for the three-body forces, a more elaborate theory will be required. One possible approach is the model recently introduced by Jayanthi *et al.*[5]

For this reason we can only attempt to quantify the experimental results by a semiempirical force-constant parametrization scheme.[48] To accurately model the phonon frequencies, we use a potential composed of a two-body part, $V^{(2)}(r_{ij})$, which depends on the distance between an atom at $\mathbf{r}_i$ and another atom at $\mathbf{r}_j$, and a three-body bending potential, $V^{(3)}(\theta_{ijk})$, to allow for the inhomogeneities of the electron gas,[49] where θ_{ijk} is the angle defined by the directions $\mathbf{r}_i$-$\mathbf{r}_j$ and $\mathbf{r}_i$-$\mathbf{r}_k$. Only by including this three-body interaction is it possible to account for the large violation of the Cauchy relations between the elastic constants C_{12} and C_{44} present in most metals.[50] With a potential of this form the force constants are of the type

$$\alpha_n = \frac{1}{r}\frac{\partial V^{(2)}}{\partial r} , \tag{4a}$$

$$\beta_n = \frac{\partial^2 V^{(2)}}{\partial r^2} , \tag{4b}$$

$$\delta_n = \frac{1}{3a_0^2}\frac{\partial^2 V^{(3)}}{\partial(\cos\theta)^2} , \tag{4c}$$

where r denotes the distance between the atom i and a nearest neighbor in the nth shell ($n=1$ refers to the first-nearest neighbor, etc.) α, β, and δ are called the tangential, radial, and three-body force constants, respectively. a_0 is the lattice constant and the factor $1/(3a_0^2)$ in Eq. (4c) is introduced to assure that δ has the same dimensions as α and β. A set of force constants for the bulk is determined by a fit to the neutron bulk-phonon dispersion curves along all symmetry directions, as well as to the measured elastic constants C_{11}, C_{12}, and C_{44}. In order to minimize the mean-square deviations, it was necessary to successively extend the two-body interactions out to fourth-nearest neighbors (4NN) and the three-body interactions out to 2NN. As seen in Fig. 11(a), this force-constant model, while providing a good fit of most of the 93 points of the bulk neutron data,[28] does not fit the Kohn anomaly in the Σ_4 branch along Γ–K. By including additional longer-range force constants out to 6NN the anomaly can also be fitted as shown in Fig. 11(b). A further increase in the number of nearest neighbors beyond six was actually found to lead to a slight increase in the mean-square deviation, so that 6NN represents the optimal fit. Thus, with a total of 14 force constants the individual bulk-phonon points[28] were fitted to better than 3%, with an average agreement of better than 1% in all regions of q space. The best-fit force constants are summarized in Table III. Note that in the procedure of force-constant parametrization used here, the translational and rotational invariance is automatically satisfied when the surface termination is introduced. This is not the case in the generalized Born–von Kármán scheme, often used to fit neutron data,[28] which is based solely on a parametrization of the force tensor.[50]

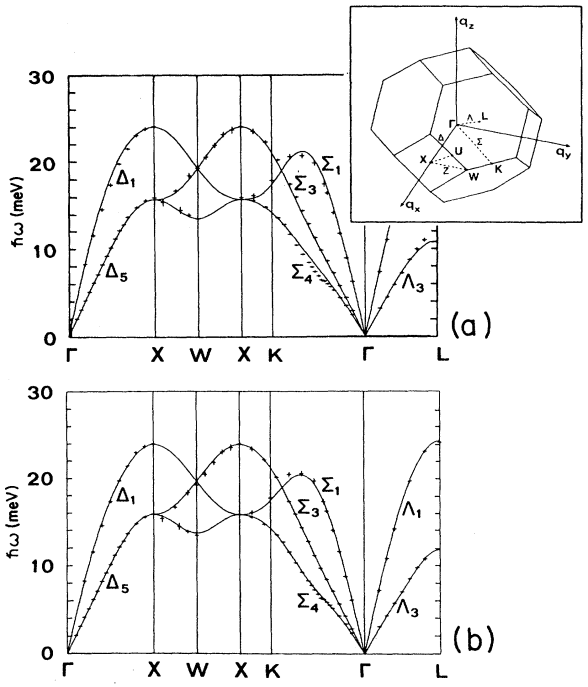

FIG. 11. Best-fit phonon dispersion curves of the bulk modes of Pt obtained from a force-constant parametrization compared with the neutron data (+) from Ref. 27 for $T=300$ K. In (a) only 4 NN interactions were included in the best fit, which, although providing a good fit to most of the curves, does not reproduce the Kohn anomaly of the Σ_4 branch along Γ–K. The NN model in (b) provides an excellent fit of the data, even in the vicinity of the Kohn anomaly in the Σ_4 branch.

The surface lattice dynamics has been simulated by the standard method of solving the dynamical matrix for a slab of N equally spaced atomic planes.[51] The solution of the $3N\times 3N$ secular problem provides the eigenmodes $\mathbf{e}(\mathbf{Q},j)$ and the frequency $\omega(\mathbf{Q},j)$ for a trial set of surface force constants. $\mathbf{e}$ is a $3N$ complex column vector for a given j that labels each of the $3N$ normal modes, where

TABLE III. Force constants for bulk Pt obtained from a best fit of the neutron data of Ref. 28 at $T=300$ K and the force constants C_{11}, C_{12}, and C_{44} with a fourth-nearest-neighbor (4NN) and a 6NN model. All force constants have units of ergs/cm^2.

	4NN			6NN		
n	α_n	β_n	δ_n	α_n	β_n	δ_n
1	1723.26	73 917.75	−3512.22	3215.3	73 730.8	−3482.9
2	−2457.23	6732.68	−743.59	−894.5	3803.7	−892.8
3	−235.29	3911.97	0	−571.0	3279.2	0
4	536.42	−4773.67	0	−427.5	−4589.4	0
5	0	0	0	−35.1	615.9	0
6	0	0	0	791.5	176.0	0

the first three components of **e** refer to the surface plane. In the present calculations, 60 atomic (111) planes with stacking *ABC* were used to ensure that interference effects between modes on the two surfaces are negligible. Since the penetration depth of the phonon in the slab is proportional to the wavelength, an interference effect can only be ruled out for surface phonons with a wave vector $Q \geq 2\pi/Nd$, where d is the interlayer spacing, which for the (111) planes is $d=a_0/\sqrt{3}$ ($a_0=3.92$ Å for Pt).

To make a direct comparison with the measured time-of-flight spectra, the one-phonon doubly differential inelastic reflection coefficients have to be evaluated. The starting formula, based on the distorted-wave Born approximation[31,52] (DWBA), is

$$\frac{d^2\sigma}{dE_f\,d\Omega}=\frac{m^2}{2\hbar^3\bar{N}Mk_{iz}}\sum_{\mathbf{Q},j}\frac{|\mathbf{k}_f|}{\omega(\mathbf{Q},j)}n(\omega(\mathbf{Q},j)) \times\left|\int dz\,\chi^*(k_{fz},z)\nabla\cdot\mathbf{U}_Q(z)\chi(k_{sz},z)\right|^2\delta(\mathbf{K}_f-\mathbf{K}_i-\mathbf{Q})\delta(E_f-E_i-\hbar\omega(\mathbf{Q},j))\ , \tag{5}$$

where m is the He atomic mass, M is the Pt atomic mass, $\bar{N}$ is the number of Pt atoms per unit area, $(\mathbf{K}_i,k_{iz})$ and $(\mathbf{K}_f,k_{fz})$ are the initial and final wave vectors of the He atom, respectively, with **K** the projection on the surface plane, and $n(\omega)$ is the Bose function, $n(\omega)=[\exp(\hbar\omega/k_BT)-1]^{-1}$. Furthermore, $\chi(k_{sz},z)$ and $\chi(k_{fz},z)$ are the translational wave functions of the He atom in the static potential of the surface, normalized to the asymptotic behavior $\chi(k_z,z)\to 2\sin(k_zz+\delta)$, where the index s refers to the specular direction. The dynamic interaction $\nabla\cdot\mathbf{U}_Q(z)$ is defined in Eq. (11) below. It is understood that both positive and negative values of $\omega(\mathbf{Q},j)$ must be included in Eq. (5), where, as in Fig. 5, positive $\omega(\mathbf{Q},j)$ correspond to phonon annihilation and negative $\omega(\mathbf{Q},j)$ correspond to phonon creation.

The He-atom–surface interaction potential that appears in the dynamic interaction $\nabla\cdot\mathbf{U}_Q(z)$ is derived from a sum of pairwise Pt-He repulsive potentials plus an attractive van der Waals potential. The procedure used in determining the potential parameters is as follows. First, we assume that the range parameter β of the assumed exponential repulsive potential can be obtained from the Esbjerg-Nørskov procedure.[53] The exponentially decreasing charge density at the surface is obtained from the superposition of the individual Pt-atom charge distributions from the tables of McLean and McLean.[54] Thus the entire He-atom–Pt-atom potential is given by

$$V(\mathbf{r})=A\rho(\mathbf{R},z)-\sum_l\frac{f_6C_6}{|\mathbf{r}-\mathbf{r}_l|^6}\ , \tag{6}$$

where $\rho(\mathbf{R},z)$ is the sum of atom charge distributions. A is 176 eV·a_0^{-3} as determined by Manninen *et al.*[55] The damping function f_6 is given by the Tang-Toennies formula[56]

$$f_6=1-\sum_{k=0}^{6}\frac{\beta|\mathbf{r}-\mathbf{r}_l|^k}{k!}e^{-\beta|\mathbf{r}-\mathbf{r}_l|}\ . \tag{7}$$

From Eq. (6) the potential between a He atom and the surface can be evaluated by considering the semi-infinite crystal as a cluster of n atomic (111) planes with N atoms per plane. To ensure convergence in the results, we take $n=15$ and $N=441$. According to the procedure described in Refs. 57 and 58 we find that we can approximate the He-atom–surface potential by

$$V(\mathbf{R},z)=U_0e^{-\beta z}\sum_l\exp\left[-\frac{\bar{\beta}|\mathbf{R}-\mathbf{R}_l|^2}{2z_t}\right]-\frac{f_3C_3}{(z-z_0)^3}\ , \tag{8}$$

where the sum is over the l atoms of the surface plane, z_t is the classical turning point,[52] $C_3=\pi C_6/6\Omega_0$ (Ω_0 being the atomic volume), and β is the softness parameter of the repulsive interaction. Notice that in Eq. (8) the **R** and z parts are decoupled and that the corrugation of the van der Waals term has been partially accounted for in the repulsive term through the effective softness parameter $\bar{\beta}$. Furthermore, the **R** dependence has a Gaussian form that produces a Gaussian lateral cutoff function in the dynamical interaction of Eq. (5). The cutoff wave vector is $Q_c=(\bar{\beta}/z_t)^{1/2}$. The parameters U_0, β, $\bar{\beta}$, and z_t are, as discussed in Ref. 58, weakly energy dependent. In the

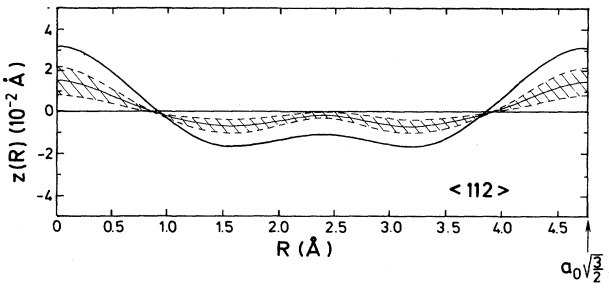

FIG. 12. Comparison of the calculated theoretical corrugation profile (solid line) evaluated from Eq. (6) for $E_i=32$ meV with the experimental corrugation (dashed line). The upper and lower bounds indicate the experimental errors.

range of incident-beam energies of interest (10–70 meV), we found[58] $U_0=14.6$ eV, $\beta=1.83$ Å^{-1}, $\bar{\beta}=2.0$ Å^{-1}, and $z_t=2.5$ Å. The value of C_6 has been taken to be slightly larger than the value quoted by Zaremba[59] in order to fit the Debye-Waller exponent measured[60] on Pt(111). The value of z_0, specifying the location of the jellium edge, has been approximated by $z_0=d/2$ (d is the interlayer spacing). In the calculations we used[58] $C_3=0.312$ eV Å^3 and $z_0=1.13$ Å. The damping function f_3 in Eq. (8) is of the same type as that used in Eq. (6) and is given by

$$f_3(x)=1-\sum_{k=0}^{3}\frac{x^k}{x}e^{-x}, \tag{9}$$

where $x=\beta(z-z_0)$. This potential gives an attractive well with a depth of 3.2 meV, which is consistent with the experimental range of values given in Ref. 60. The corrugation profile obtained from this potential along the $\langle 112\rangle$ direction at $E_i=32$ meV is depicted in Fig. 12 together with the corrugation obtained from the diffraction experiments as discussed in Sec. III. The dashed area connects the upper and lower bounds on the experimental corrugation parameters given in Table II. The theoretical results overestimate the experiment by about a factor of 2. This can be considered to be reasonably good agreement since the theoretical potential has a soft repulsive wall, whereas the experimental data were evaluated assuming a hard corrugated wall.

For the DWBA calculation of inelastic one-phonon intensities, we also need the laterally averaged potential derived from Eq. (8), defined by

$$V_0(z)=\frac{1}{A_c}\int d^2R\ V(\mathbf{R},z)$$
$$=\frac{2\pi U_0}{A_c Q_c^2}e^{-\beta z}-\frac{C_3}{(z-z_0)^3}f_3(\beta(z-z_0)), \tag{10}$$

where A_c is the surface unit-cell area. Consistent with the previous assumptions the dynamical interaction is well approximated by

$$\nabla\cdot\mathbf{U}_Q(z)=\frac{2\pi U_0}{A_c Q_c^2}\bar{N}[i\mathbf{Q}\cdot\mathbf{e}_L(\mathbf{Q}_{ij})-e_z(\mathbf{Q},j)\beta]$$
$$\times\exp(-\beta z)\exp(-\tfrac{1}{2}Q^2/Q_c^2), \tag{11}$$

where $\mathbf{e}_L$ and e_z are the longitudinal and vertical components of the polarization vector of the surface atoms and the cutoff wave vector is $Q_c=0.9$ Å^{-1} for Pt.[58]

Inserting these expressions in Eq. (5) and integrating over $\mathbf{Q}$, we obtain

$$\frac{d^2\sigma}{dE_f\,d\Omega}=\frac{m^2}{2\hbar^3 M A_c Q_c^4 k_{iz}}\sum_j|\mathbf{k}_f|\,|\langle\chi(k_{fz},z)|U_0\exp(-\beta z)|\chi(k_{iz},z)\rangle|^2 n(\omega(\mathbf{Q},j))$$
$$\times e^{-(Q/Q_c)^2}\frac{|-\beta e_z+i\mathbf{Q}\cdot\mathbf{e}_L|^2}{\omega(\mathbf{Q},j)}\frac{\delta(E_f-E_i-\hbar\omega(\mathbf{Q},j))}{J(\mathbf{Q},j)}, \tag{12}$$

with $\mathbf{Q}=\mathbf{K}_f-\mathbf{K}_i$. The $\chi(z)$ are the eigenfunctions of the laterally averaged potential of Eq. (8), and the cutoff function $e^{-(Q/Q_c)}$ accounts for the finite effective range of the He-atom–surface interaction potential.[61] Thus, as the range of the potential increases, several surface atoms will be deflected simultaneously and the excitation of short-wave phonons will be impaired. This cutoff effect, commonly called the Armand effect,[62] is accounted for by the parameter Q_c. In the case of smooth metal surfaces it strongly reduces the intensity of scattering events outside the first Brillouin zone. The Jacobian J, which arises from the conservation of momentum imposed by the δ function in Eq. (5), is given by[63]

$$J(\mathbf{Q},j)=1-\frac{\mathbf{K}_f\cdot\nabla\hbar\omega(Q,j)}{2E_f}. \tag{13}$$

To account for the finite resolution of the apparatus, the energy δ function in Eq. (5) is represented by the normalized Gaussian

$$\delta(E_i+\hbar\omega(\mathbf{Q}_j)-E_F)\rightarrow\frac{4\ln 2}{\pi}\frac{e^{-4\ln 2\left[\frac{E_i+\hbar\omega(\mathbf{Q},j)-E_f}{\Delta E}\right]^2}}{\Delta E}, \tag{14}$$

where ΔE is the full width at half maximum of the experimental resolution function $\Delta E=0.2$ meV. In our experiments, which for reasons of resolution are restricted to creation events, the major source of smearing is from the finite width of

the incident beam, $\Delta E_i/E_i \cong 1.5\%$.[24,64] The observed reflection coefficient is obtained by integration of Eq. (12) over E_i using Eq. (14):

$$\frac{d^2\sigma}{dE_f\,d\Omega} = \frac{m^2}{2\hbar^3 M A_c Q_c^4} \sum_j \int d\bar{E}_i\, f_i(E_i-\bar{E}_i)\frac{|k_f|}{|k_{iz}|} n(\omega(\mathbf{Q},j)) e^{-(Q/Q_c)^2} \times |\langle \chi(k_{fz};z)|U_0 \exp(-\beta z)|\chi(k_{iz},z)\rangle|^2 \frac{|-\beta e_z(\mathbf{Q},j)+i\mathbf{Q}\cdot\mathbf{e}_L(\mathbf{Q},j)|^2}{\omega(\mathbf{Q},j)J(\mathbf{Q},j)} \times \frac{4\ln 2}{\pi}\frac{e^{-4\ln 2\left[\frac{E_i+\hbar\omega(\mathbf{Q},j)-E_f}{\Delta E}\right]^2}}{\Delta E}, \tag{15}$$

where we have used a Gaussian $f_i(E_i-\bar{E}_i)$ to account for the initial beam-energy spread ΔE_i. The integration is especially important in the vicinity of a kinematic focusing situation,[25–27] which was avoided in these measurements. Kinematical focusing occurs when the scan curve $\omega=\omega_s(\mathbf{Q},E_f,E_i,\theta_f)$ determined by the conservation of energy and parallel momentum is tangent to a phonon branch $\omega=\omega(\mathbf{Q},j)$. In this case the Jacobian goes to zero and a singularity arises at $E_i=\bar{E}_i$. By expanding the Jacobian in terms of $E_i-\bar{E}_i$, it can be shown that

$$J\sim(E_i-\bar{E}_i)^{1/2}\ .$$

This square-root singularity present in the reflection coefficient is washed out by the integration over $\bar{E}_i$ in Eq. (15). Thus, at kinematic focusing the averaged reflection coefficient exhibits a broad peak.

V. COMPARISON OF EXPERIMENT WITH THEORY

A. Clean platinum surface

As discussed above, the He-atom–surface potential influences the intensities of the individual peaks in the time-of-flight spectra. Thus, before applying the theory to evaluations of the measured time-of-flight spectra, it is necessary to verify the validity of the atom-surface potential used. Figure 8 shows a comparison of the theoretical calculation of the Rayleigh-mode intensities with the measured intensity of the coherent peak in the experimental spectra. The overall agreement confirms the applicability of the potential. For sake of convenience, we assumed that the same potential can also be used to simulate the phonons on the hydrogen-covered surface.

Figure 13 shows a comparison of experimental time-of-flight spectra for the $\bar{T}\langle 110\rangle$ direction with time-of-flight spectra evaluated using the unmodified bulk force constants of Table III. Note that for this comparison a somewhat different set of spectra than those presented in Fig. 6 was chosen. It is seen that this calculation can duplicate the experimental results at small Q [Figs. 13(a) and 13(b)], but provides a progressively poorer description as Q increases, with very large deviations, especially in Figs. 11(l) and 11(i). An analysis of the polarization vectors corresponding to the calculation in Fig. 13 reveals that, at small Q, two surface modes, the Rayleigh mode and another, a pseudo-Rayleigh mode known from the continuum theory of elasticity, are present.[65] This latter mode, which arises from the lack of inversion symmetry with respect to the sagittal plane,[66] penetrates deeply into the bulk. In Al(111) and Au(111) the pseudo-Rayleigh mode has been observed by surface laser Brillouin scattering at the zone origin by Sandercock.[67] Another consequence of the breakdown of symmetry is that the shear and sagittal displacement components become mixed and the mode that would otherwise be pure shear horizontal and invisible to particle scattering acquires a sagittal component and can, in principle, therefore, be detected.

These model calculations show that the pseudo-Rayleigh wave broadens at larger momentum transfer into a wide resonance and finally disappears into the bulk density of states. Thus, at larger Q the calculated struc-

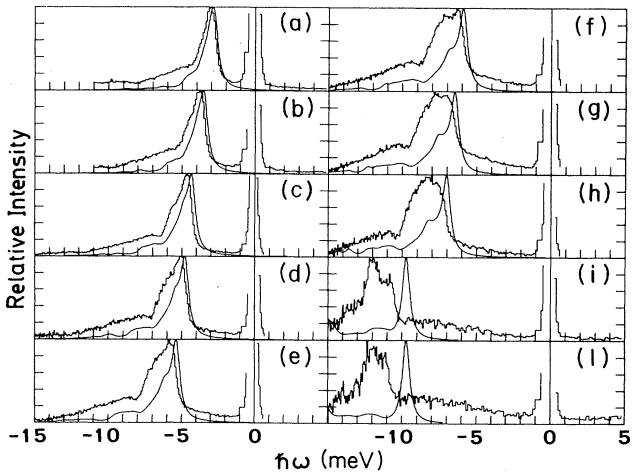

FIG. 13. Comparison of calculated time-of-flight spectra for clean Pt(111) with the experimental results for the $\bar{T}\langle 110\rangle$ direction. The calculations are based on bulk force constants obtained from a best fit of the bulk dispersion curves and elastic constants. They have not been modified to fit the surface-phonon data. The experimental conditions are $E_i=24.4$ meV and $\theta_{SD}=90°$; the incident angles are (a) $\theta_i=41.48°$, (b) $\theta_i=40.52°$, (c) $\theta_i=39.24°$, (d) $\theta_i=38.50°$, (e) $\theta_i=37.52°$, (f) $\theta_i=36.51°$, (g) $\theta_i=35.50°$, (h) $\theta_i=34.50°$, (i) $\theta_i=28.00°$, and (l) $\theta_i=27.00°$. The solid line represents the calculated averaged reflection coefficients, and the histograms show the experimental data. Note the increasingly large discrepancies near the zone border.

ture is dominated by the Rayleigh mode and also the edge of the transverse bulk band, which produces the first small secondary peak at larger energy transfer in the theoretical spectra. The remaining structure at larger energy transfer is due to interactions with the bulk bands.

The very large discrepancies found between theory and experiment in Fig. 13 indicates without a doubt that the unmodified bulk force constants are not able to explain the experiments. The theory not only fails to predict the correct frequencies of the Rayleigh mode, but is also unable to properly account for the additional structure and large width of the inelastic peak, especially at large energy transfer. The latter observation strongly suggests the presence of a longitudinal anomaly very similar to that previously observed in the noble metals.[1–3] The explanation of the anomalies in the noble metals is that the force constants at the surface are reduced compared to the bulk values.[4,49,68] Since the $5d$ shell of Pt has only one less electron than the full shell in Au, we might indeed expect Pt to behave much in the same way as a noble metal.

As in the noble metals, the fit was carried out by a trial-and-error procedure, starting with a variation of the first-nearest-neighbor central force constant $\beta_1^{\parallel}$, where the superscript $\parallel$ indicates that β describes only the lateral interactions within the surface plane. The radial force constant describing the interaction between the first two planes, $\beta_1^{\perp}$, is, however, maintained at the bulk value. This modification already leads to the appearance of a third mode, which from the polarization vector can be assigned to the longitudinal resonance LR along the $\bar{T}\langle 110\rangle$ direction. This is the same resonance first observed in calculations of the Ag(111) surface.[4] In the present case it was also necessary, however, to adjust α_1 and δ_1 in the surface layer in order to get the correct relative peak heights and energy positions in the time-of-flight spectra. The final best-fit values of α and δ obtained after many iterations are $\alpha_1^{\parallel}=1.7\alpha_1^b$ and $\delta_1^{\parallel}=0.037\delta_1^b$ (see Table IV). A physical interpretation of these force-constant modifications will be presented in Sec. VI.

In Figs. 14 and 15 we compare the time-of-flight spectrum calculated for the best-fit set of force constants with the experimental results for the $\bar{T}\langle 110\rangle$ and $\bar{\Sigma}\langle 112\rangle$ directions, respectively. The solid bars in the theoretical spectra show the reflection coefficients evaluated for a sharp distribution of incident and final energies, and in this way clearly show the different modes present and how they would appear in an ideal apparatus. The smooth curves have been averaged so as to simulate the actual experimental conditions. The overall agreement between experiment and theory is very good. It should be particularly noted that the initial rise in the time-of-flight peaks agree with experiment to within ≤ 0.1 meV. This is comparable to the root-mean-square deviation claimed earlier for an experimental fit to the position of the Rayleigh mode.[6] In both the experimental and theoretical (smooth) spectra of Figs. 14(g)–14(i), two distinct maxima and a weak shoulder on the left-hand side of the main structure can be seen. Although all three peaks are not resolved, the good agreement between theory and experiment provides convincing evidence that the additional mode arising from the lateral softening of surface interactions is indeed present in addition to the Rayleigh and pseudo-Rayleigh modes.

TABLE IV. Surface force constants for the surface layer obtained in the present work from a 6NN best fit of the helium surface-phonon dispersion curves and relaxation data. Also listed are the ratios to the corresponding bulk values. The force constants have the same units as in Table III.

Force constant	Value from surface phonons	Value from relaxation[a]	Ratio to bulk value
$\alpha_1^{\parallel}$	1363.1	bulk value	1.7
$\alpha_1^{\perp}$	bulk value	4179.9	1.30
$\beta_1^{\parallel}$	29 009.0	bulk value	0.39
$\beta_2^{\perp}$	bulk value	bulk value	1.00
$\delta_1^{\parallel}$	128.93	bulk value	0.037
$\delta_1^{\perp}$	bulk value	bulk value	1.00

[a]See Sec. VI. The change in $\alpha_1^{\perp}$ needed to maintain the correct experimental relaxation of 0.4% has no effect on the surface-phonon frequencies.

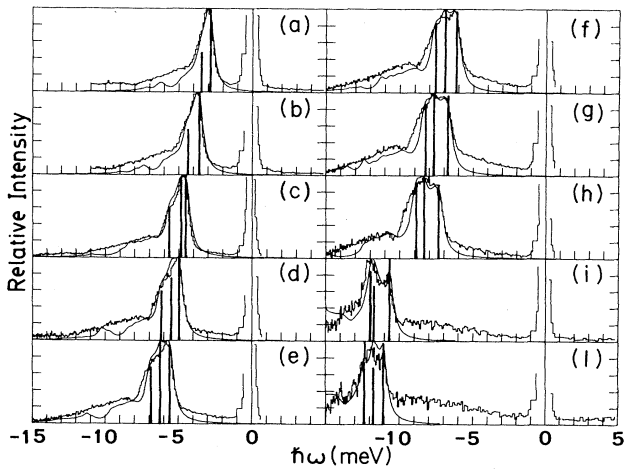

FIG. 14. Comparison of calculated time-of-flight spectra for clean Pt(111) with the experimental results for the $\bar{T}\langle 110\rangle$ direction. The calculations are based on the best-fit force constants of Table IV, which have been modified in the surface layer. The experimental conditions are $E_i=24.4$ meV and $\theta_{SD}=90°$; the incident angles are (a) $\theta_i=41.48°$, (b) $\theta_i=40.52°$, (c) $\theta_i=34.24°$, (d) $\theta_i=38.50°$, (e) $\theta_i=37.52°$, (f) $\theta_i=36.51°$, (g) $\theta_i=35.50°$, (h) $\theta_i=34.50°$, (i) $\theta_i=28°$, and (l) $\theta_i=27°$. The solid line represents the calculated averaged reflection coefficients and the histograms show the experimental data. The vertical heavy lines are the scattering intensities, calculated from Eq. (15) of the R, PR, and LR modes for an ideal apparatus. In spectra (c)–(h), the ordering of the modes in order of increasing energy transfer is R, PR, and LR. For spectra (i) and (l) the ordering is R, LR, and PR. For spectra (a) and (b) only the R and PR orders are present.

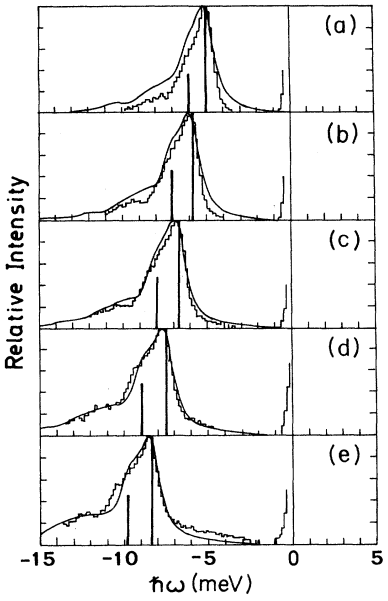

FIG. 15. Comparison of calculated time-of-flight spectra for clean Pt(111) with the experimental results for the $\bar{\Sigma}$ ⟨112⟩ direction. The calculations are based on the best-fit force constants of Table IV, which have been modified in the surface layer. The experimental conditions are $E_i=31.2$ meV and $\theta_{SD}=90°$; the incident angles are (a) $\theta_i=40°$, (b) $\theta_i=39°$, (c) $\theta_i=38°$, (d) $\theta_i=37°$, and (e) $\theta_i=36°$. The solid-line curve represents the calculated averaged reflection coefficients. The histograms show the experimental data. The vertical heavy lines are the scattering intensities, calculated from Eq. (15), of the R and LR modes with increasing energy transfer, respectively, for an ideal apparatus.

On the basis of an analysis of the polarization vectors of the three modes observed for angles θ_i down to 34.5° in Fig. 14, we assign the lowest in frequency to the Rayleigh mode (R), the intermediate one to the pseudo-Rayleigh mode (PR), and the highest-frequency mode to the longitudinal resonance. At small Q corresponding to θ_i near the specular angle of 45°, the R mode is dominant. With increasing Q, corresponding to decreasing θ_i, in this case, the intensities of both the PR and LR modes increase and their energy separation decreases. At $\theta_i=28°$ the frequencies of both modes are nearly the same. Since both modes have substantial longitudinal components, they hybridize at the value of Q corresponding to this angle. At $\theta_i=27°$, beyond the region of hybridization, one again notices the presence of the three well-separated modes. However, the ordering is now reversed, with the LR mode having a lower energy than the PR mode. Notice that the intensity of the LR mode increases relative to Rayleigh mode. This can be explained by the factor **Q** by which $\mathbf{e}_L$ is multiplied in Eq. (15). In Fig. 14 it is also seen that observable structures with energy transfer greater than the three surface modes are also well fitted by the calculations. They can be attributed to the high density of the surface-projected bulk-phonon states, as will be discussed in Sec. VI.

It is interesting to note that the Rayleigh mode for the best-fit calculations in Fig. 14 actually lies higher in frequency by about 2.5 meV near the zone boundary than the Rayleigh mode calculated for the bulk force constants presented in Fig. 12. This upward shift in the Rayleigh-mode frequency can be attributed to the adjustment of the tangential force constant $\alpha\|$ at the surface, which affects the transverse frequency in the region of the zone boundary.

Along the $\bar{\Sigma}$ ⟨112⟩ direction the best-fit agreement between the calculations for the same set of modified force constants and experiment is also very good, as shown in Fig. 15. In this case the theory predicts only two peaks, one of which is the Rayleigh mode and the other the longitudinal resonance. Even though the two peaks are not always separated (see also Fig. 4), the very good agreement between experiment and theory can be regarded as good evidence for the presence of the two modes.

Figure 16 shows the calculated dispersion curves for an $N=60$ layer slab with the modified force constants. The top panel shows also the dispersion curves where the different symmetries of the modes are distinguished by dashed and solid lines. The dashed lines in the $\bar{\Sigma}$ direction indicate shear horizontal modes. In the $\bar{T}$ direction the dashed lines indicate odd modes with respect to the central plane of the slab. Note that in the $\bar{T}$ direction there is no other symmetry. The solid lines indicate the sagittal modes in the $\bar{\Sigma}$ direction and even modes in the $\bar{T}$ direction. It is interesting to observe that along the $\bar{T}$ ⟨110⟩ direction the lower edges of the bulk bands agree exactly with the bulk dispersion curves Σ_4, Σ_3, and Σ_1 modes in the $\bar{\Gamma}$–$\bar{X}$ direction shown in Fig. 11. Note that the reciprocal-lattice distance in the bulk along Γ–K–X–W is equivalent to the $\bar{\Gamma}$–$\bar{K}$–$\bar{M}$ distance at the surface. The bottom panels in Fig. 16 show only the dispersion curves of those surface modes and resonances with a large density of states in the surface layer. These are the modes seen in the experiment. A direct comparison of experimental and theoretical curves is only possible for the $\bar{\Sigma}$ direction since the resolution was not good enough to separate the three curves in the $\bar{T}$ direction.

One interesting peculiarity of the Pt(111) surface is found in the $\bar{T}$ ⟨110⟩ direction. As shown in Fig. 16, the Rayleigh mode is not distinctly separated from the transverse polarized bulk band edge for $Q<1.2$ Å^{-1}. Only at very small $Q<0.1$ Å^{-1} is the Rayleigh mode slightly below the bulk band edge. This cannot be seen in Fig. 15, but is evident from the fact that the velocity of sound at the surface evaluated for an elastic semi-infinite medium is 98.5% of the transverse bulk velocity. In the intermediate region, where the bulk band edge dips downward, the Rayleigh mode is actually a surface *resonance* and not a surface *mode*.

Previously[6] the undulatory form of the lower transverse band edge at the surface along the $\bar{T}$ ⟨110⟩ direction was attributed to a surface Kohn anomaly, which, in the bulk, has been observed by neutron scattering in the Σ_4 branch[28] (see Fig. 11). In the earlier experimental analysis of the time-of-fight spectra, we did not have at our disposal the best-fit lattice-dynamical calculations

presented here. Instead, we analyzed the spectra in terms of what appeared to be only two maxima. To determine the location of the Rayleigh dispersion curve, the initial rise in the spectra was fitted by a Gaussian distribution with adjustable width. The so-determined Rayleigh curve was found to show anomalous behavior, which is best represented by plotting the group velocity (the local slope of the dispersion curve) as a function of the wave vector. To obtain smooth curves, the experimental points were first fitted to a Fourier expansion

$$\omega_{\mathrm{RW}}^2 = \sum_{n=1}^{8} A_n [1-\cos^2(n\pi Q/Q_{\mathrm{BZ}})] \ . \tag{16}$$

The result of this previous data analysis is shown by the dashed line in Fig. 17. This previous interpretation of the data is to be compared with the group velocity of the Rayleigh wave, determined from the present theoretical best fit. The resulting curve is shown by the solid line in Fig. 17. It is gratifying to see that the new theoretical fit confirms the presence of an anomaly with a minimum at

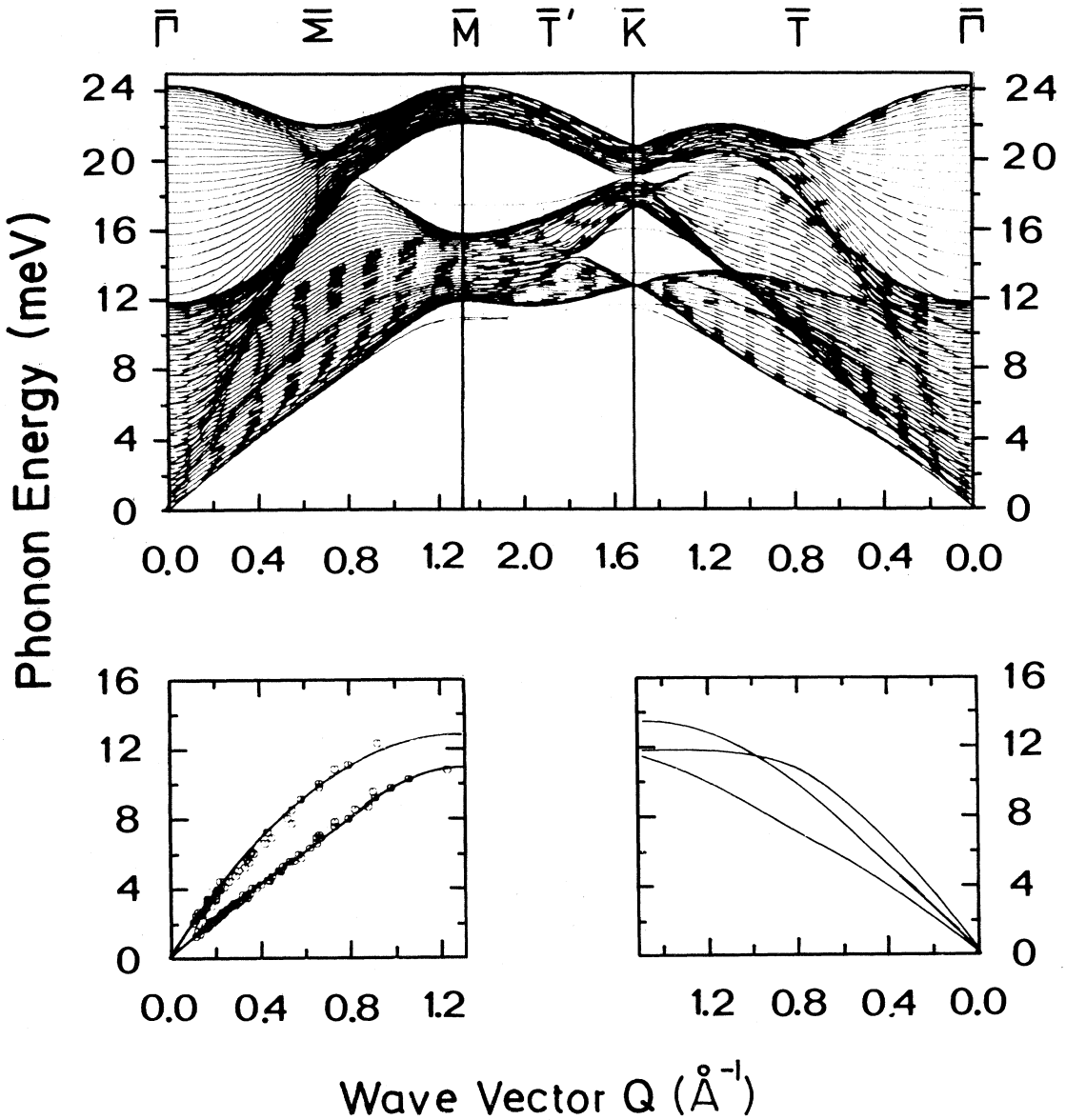

FIG. 16. (a) Dispersion curves for clean Pt(111) with Q along the high-symmetry directions of the two-dimensional Brillouin zone, calculated with a slab of 60 atomic planes. The dashed lines in the $\bar{\Sigma}$ direction indicate shear horizontal modes. In the $\bar{T}$ direction the dashed lines indicate odd modes with respect to the central plane of the slab. Note that in the $\bar{T}$ direction there is no other symmetry. The solid lines represent the sagittal modes in the $\bar{\Sigma}$ direction and the even modes in the $\bar{T}$ direction, where there are pure sagittal modes. (b) The bottom two panels show the dispersion curves of the localized and resonant surface modes, obtained from the best-fit reflection coefficients. Experimental data are only shown for the $\bar{\Sigma}$ direction since the location of the two peaks can only be extracted from the data for this direction.

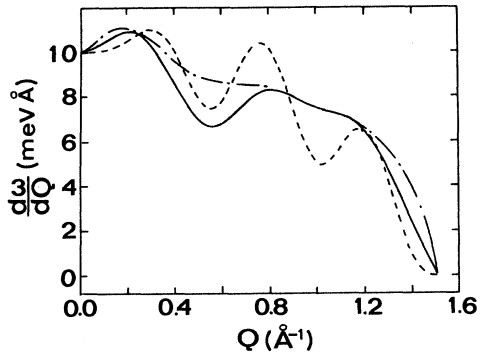

FIG. 17. Group velocity of the Rayleigh peak as a function of Q along the $\bar{T}\langle 110\rangle$ direction. The dashed line represents the experimental group velocity determined from the Rayleigh-mode dispersion curve (Ref. 6). The solid line indicates the theoretical determination of the group velocity from the best-fit 6NN force constants and the dotted-dashed line shows the theoretical group velocity for a 4NN model, which does not show the Kohn anomaly (Ref. 6).

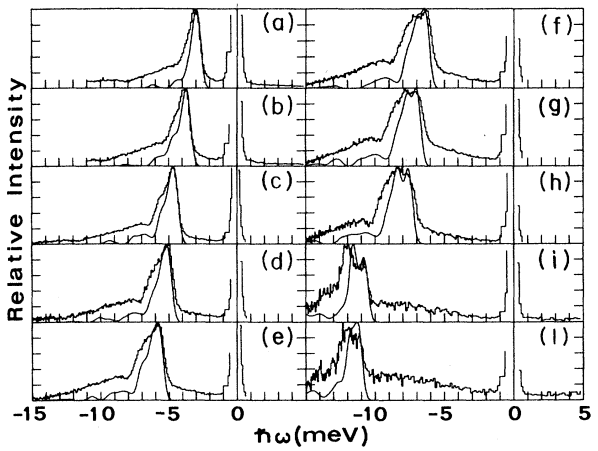

FIG. 18. Same experimental spectra as in Fig. 14. The solid lines refer to the calculations performed with the 4NN bulk-phonon model, which accurately reproduces the bulk-phonon branches, except for the Kohn anomaly in the Σ_4 branch.

a wave vector of about 0.55 Å^{-1}. The new fit does not, however, reveal the presence of a second anomaly with a minimum at $Q=1.00$ Å^{-1}, reported earlier. Indeed, this second anomaly was only very slight and may easily have been erroneously produced by the previous fitting procedure. Also, we must now regard the reported anomalous broadening of the Rayleigh peak, which was thought to set in at $Q=0.6$ Å^{-1} and extend up to about 1.2 Å^{-1}, as spurious. Presumably, it resulted from the incorrect assumption of only two peaks.

With the availability of the theoretical simulation, we can study the effect of the force-constant model on the appearance of the Kohn anomaly. As shown previously, a force-constant model with only 4NN and angle-bonding forces (a total of 10 force constants) can fit the bulk data almost as well, except for the Kohn anomaly, which is smoothed over. The surface force constants were fitted to the time-of-flight spectra and were found to be very similar to those reported in Table IV with, in this case, $\alpha_1^{\parallel}=1.6\alpha^b$, and $\beta_1^{\parallel}=0.39\beta^b$. The dotted-dashed curve in Fig. 17 shows the group velocity of the Rayleigh wave and confirms the absence of the anomaly, but otherwise shows good agreement with the more detailed fit. Figure 18 compares the time-of-flight spectra. It is seen that in the region of the initial rise this theory agrees well with the experimental data for spectra (a)–(c) and (i) and (l), corresponding to the ranges $Q=0.2$–0.35 Å^{-1} and $Q\geq 1.25$ Å^{-1}, respectively. In the intermediate region, however, the theoretical spectra predict an initial rise at energies that are shifted upward by about 0.3 meV compared to the experiment. This small shift is just the extent of the previously reported experimentally observed depression in the Rayleigh frequency due to the surface Kohn anomaly. Despite the apparent good agreement between experiment and theory, the definite confirmation of the existence of a surface Kohn anomaly must await further, better-resolved experiments. This calculation suggests that if a surface anomaly exists near $Q\cong 0.55$ Å^{-1}, it is probably merely a projection of the bulk anomaly onto the surface. This pretty much rules out the possibility of an anomaly due to the coupling of the surface phonons to surface-electronic states as conjectured previously.[6]

The broad peaks observed at higher-energy transfers in some of the TOF spectra in Figs. 6 and 14 appear to be associated with the high density of states near the second transverse threshold and the longitudinal threshold. These modes are found, in the calculations, to have a large component of the displacement field in the sagittal plane. In other measurements on Pt(111) these broad peaks have received special notice.[8] Since these structures merely reflect known bulk properties, they do not provide new information on the surface.

From Eq. (15) it is clear that interference between the components $\mathbf{e}_L$ and $\mathbf{e}_z$ of the surface modes can play an important role. For instance, by cutting the crystal along a direction nearly normal to the (111) direction, the stacking of the planes becomes *ACB*, whereas *ABC* is the stacking related to the (111) surface as shown in Fig. 1. In this new geometry the second plane is rotated by 180° with respect to the second plane of the *ABC* stacking. This rotation transforms the dynamical matrix into its Hermitian conjugate, so that, although the eigenvalues remain the same, the polarization vectors change over to the complex-conjugate values. In this way the sign of the interference term in the square modulus of Eq. (15), which contains the polarization vector $\mathbf{e}$, is also affected. The predicted effect of the stacking differences on the TOF spectra is shown in Fig. 19. The solid line represents the calculation for the *ABC* stacking, and the dashed curve refers to the *ACB* stacking. As one can see, the scattering intensity of the longitudinal resonance in *ACB* stacking is much larger than that of the Rayleigh and pseudo-Rayleigh peaks. Thus, we can conclude *a posteriori* that our experiments were performed on a crystal with *ABC* stacking. This dynamical analysis reveals that the crystallographic orientation of the surface can have a strong effect on the time-of-flight spectra. In

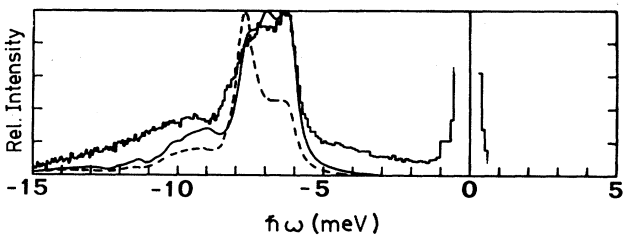

FIG. 19. Two calculated time-of-flight spectra, with Q along the $\bar{T}\langle 110\rangle$ direction, for $E_i=24.40$ meV and $\theta_i=35.50°$, compared with the measured histogram. The solid line represents the calculation performed for the Pt(111) surface with *ABC* stacking, while the dashed line refers to the Pt(111) surface with *ACB* stacking.

another recent study of one-phonon inelastic TOF spectra from the reconstructed Au(111) surface, we also found that the geometry of the second layer can noticeably influence the time-of-flight spectra.[69]

B. Pt(111)+H(1×1) surface

The Pt(111)+H(1×1) time-of-flight spectra were simulated in the same way as the clean Pt(111) surface. In these calculations the clean-surface lattice structure was assumed, and the vibrations of the hydrogen atoms were neglected since they lie much higher in frequency. The effect of the hydrogen atoms on the platinum-atom vibrational frequencies can also be neglected since the hydrogen atom has less than 1% the mass of the Pt atom (195 amu), and therefore is expected to reduce the frequency at the zone boundary by less than 0.5%. The neglect of the hydrogen mass has also been confirmed experimentally by measurements on the deuterium-covered surface, which showed the same Rayleigh phonon frequencies within experimental errors. Chemisorbed hydrogen was observed to have practically no effect on the rotational Feshbach resonances observed in the scattering of HD from the clean surface,[70] suggesting that the potential wells in both cases are about the same. This suggests that the He-surface potential will also be the same as for the clean surface. The only apparent major change in the surface potential is the increase in corrugation discussed in Sec. III.

As with the clean Pt surface, we first tried to fit the surface phonons using the bulk force constants. Surprisingly, they provide, without further modification, a very good fit of the measured time-of-flight spectra as shown in Figs. 20 and 21. Figure 22 shows the dispersion curves calculated for the bulk force constants and shows a direct comparison with the location of the single peak in the time-of-flight spectra. Note that the bulk bands are exactly the same as for the clean surface shown in Fig. 16, the only difference being in the surface resonances and modes. The overall agreement with experiment is good, although there are some small discrepancies, especially in the $\bar{T}\langle 110\rangle$ direction. For example, for $Q<1.1$ Å^{-1} the experimental points lie above the Rayleigh curve. One possible explanation is that unresolved contributions

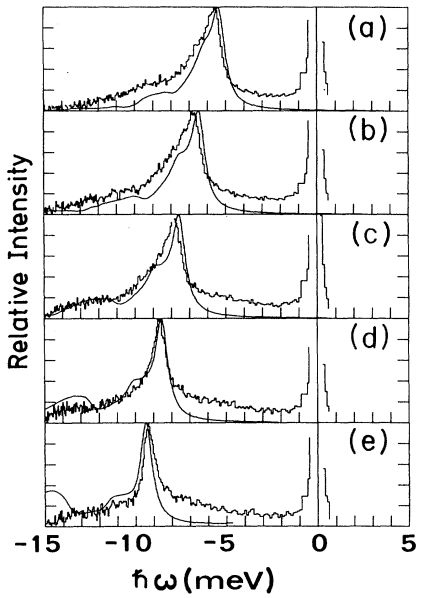

FIG. 20. Comparison of theoretical and experimental time-of-fight spectra for Pt(111)+H(1×1) with Q along the $\bar{T}\langle 110\rangle$ direction for $E_i=24.4$ meV: (a) $\theta_i=37.49°$, (b) $\theta_i=35.51°$, (c) $\theta_i=33.49°$, (d) $\theta_i=31.55°$, and (e) $\theta_i=29.49°$. The solid line represents the calculated averaged reflection coefficients. The histogram represents the experimental data.

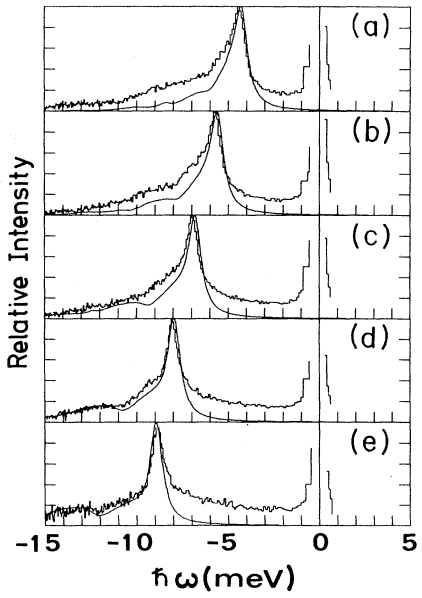

FIG. 21. Comparison of theoretical and experimental time-of-flight spectra for Pt(111)+H(1×1) with $Q\langle 112\rangle$ along the $\bar{\Sigma}$ direction, for $E_i=24.40$ meV, and (a) $\theta_i=39.50°$, (b) $\theta_i=37.50°$, (c) $\theta_i=35.50°$, (d) $\theta_i=33.50°$, and (e) $\theta_i=31.50°$. The solid line represents the calculated averaged reflection coefficients. The histogram represents the experimental data.

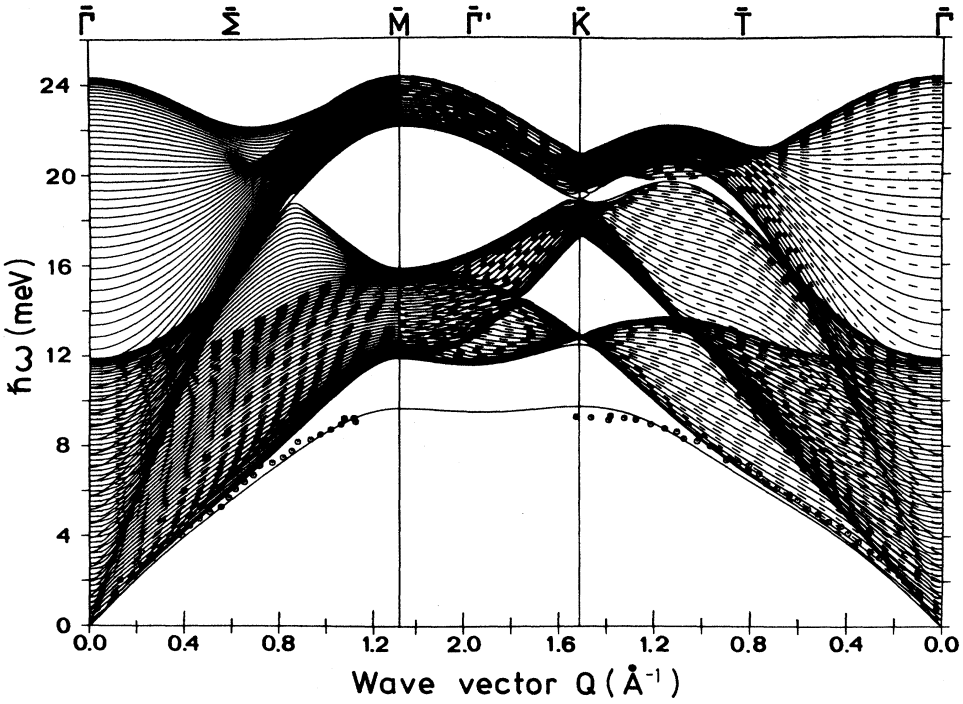

FIG. 22. Comparison of the measured dispersion curves for the Pt(111)+H(1×1) surface with the results of a lattice-dynamical calculation with unmodified bulk force constants for a slab of 60 atomic planes. The meaning of the dashed and solid curves is the same as in Fig. 16.

from the surface and the bulk band edges lead to a shift of the center of the measured peak to slightly higher energies. The theoretical spectra of Figs. 20(d) and 20(e) show a bump at around −15 meV. This is an artifact of the calculations, and an increase in the thickness of the slab would dramatically reduce the height of this structure. Aside from these small differences the hydrogen-covered surface shows all the dynamical features of a simple termination of the bulk. Note that the Rayleigh mode for the hydrogenated surface is lower by 1.5 meV than for the clean, but dynamically modified, surface. For this reason the calculated Rayleigh mode is clearly separated from the transverse bulk band edge, as is apparent from Fig. 22.

VI. SUMMARY AND DISCUSSION

The lattice-dynamical analysis has enabled us to not only identify, but also to quantitatively analyze, the experimental surface-phonon dispersion curves. Along the $\bar{\Sigma}\langle 112\rangle$ direction the polarization vectors of the best-fit modes indicate that, in addition to the Rayleigh mode, an anomalous longitudinal mode is present, whereas in the $\bar{T}\langle 110\rangle$ direction both an additional anomalous longitudinal and a pseudo-Rayleigh mode are present. These results show that the forces at the surfaces of transition metals have strong similarity with the noble metals, where the anomalous longitudinal resonance was first found. If we extend this analogy further it appears very likely that for the noble metals there will also be a more complex interplay between the longitudinal resonance and pseudo-Rayleigh modes along the $\bar{T}\langle 110\rangle$ direction. This was not clear from the original theoretical analysis of the Ag(111) experiments, but did show up in the extensive fits of the Au(111) surface. However, Au(111) shows a number of peculiarities with regard to the other noble metals. A similar detailed analysis is presently in progress for Cu and will shed more light on the nature of the coupling of the LR and PR modes.

Here it must be mentioned that the satisfactory fit of all the surface dispersion curves in both directions could only be achieved by using, as a starting point, an extensive set of force constants for both two-body radial and tangential force constants, including interactions to six nearest neighbor as well as second-nearest-neighbor three-body terms as obtained from a best fit of the bulk data. At least three of these constants describing forces within the surface plane had to be extensively modified in order to fit the surface-phonon dispersion curves. Note that by modifying the tangential force constants at the surface, the effects of surface stress are fully accounted for. In a simple nearest-neighbor interaction model it can be shown that $\gamma=\frac{1}{2}\alpha\|$, where γ is the stress in the surface layer.[71]

Unfortunately, this force-constant parametrization scheme is not directly related to the true intermolecular forces in the metal or at its surface. As discussed at the beginning of Sec. IV, the physical understanding of the forces between atoms at the surface or, for that matter, even in the bulk, is still largely lacking. Theory explains these forces in terms of the electronic densities in the lattice and, with some effort, the individual terms can be

provided with a physical interpretation.[72] *Ab initio* calculations have been performed for a few bulk systems[38] and for surface phonons on Al(110),[46] but unfortunately, these calculations do not usually provide a simple physical interpretation. In view of this situation one can view the force-constant parametrization procedure adopted here as a way to transform the phonon momentum-space information into local coordinate space. With this information on the force constants in hand, we will now attempt to obtain physical insight into the interactions between the individual atoms at the surface.

In addition to having explicit values for the force constants on the clean and hydrogen-covered surfaces, we also have additional information on the surface atomic forces coming from the geometrical relaxation of the Pt(111) surface. First, we note that the calculations based on the unmodified bulk force constants predict a contraction of the distance between the first two layers by about $\sim 3\%$, which can be compared with the current experimental estimates of about $0\pm 0.4\%$ (Ref. 35) and an expansion of about $+1.3\pm 0.4\%$ for the hydrogen-covered surface.[35] Within the force-constant parametrization scheme, the increase in the surface layer spacing from -3% contraction to a 0% change can be reproduced by increasing the tangential force constant between the layers, $\alpha_1^{\perp}$, by about 30%. This force-constant change has, however, practically no effect on the observable surface-phonon frequencies, as indicated by additional calculations.[73] Thus, consideration of relaxation leads to an additional modification of the force constants; this time, however, an interplanar force constant is affected.

In general, the relationship between frequencies and force constants is rather complicated. For the zone-boundary frequencies it has nevertheless been possible to arrive at nearly exact analytic expressions. These are illustrated by the following approximate results in which only nearest-neighbor interactions are included:[74]

$$\text{transverse vertical mode at } \bar{M}\text{: } \omega_z^2=\frac{2}{M}(3\beta_1^{\parallel}+\alpha_1^{\parallel}+9\delta_1^{\parallel})+\text{interplanar terms}, \tag{17a}$$

$$\text{transverse vertical mode at } \bar{K}\text{: } \omega_z^2=\frac{9}{M}\alpha_1^{\parallel}+\text{interplanar terms}, \tag{17b}$$

$$\text{longitudinal resonance at } \bar{K}\text{: } \omega^2=\frac{9}{2M}(\beta_1^{\parallel}+\alpha_1^{\parallel}+\tfrac{9}{2}\delta_1^{\parallel})+\text{interplanar terms}, \tag{17c}$$

$$\text{pseudo-Rayleigh mode at } \bar{K}\text{: } \omega^2=\frac{9}{2M}(\beta_1^{\parallel}+\alpha_1^{\parallel}+\tfrac{9}{2}\delta_1^{\parallel})+\text{interplanar terms}, \tag{17d}$$

where M is the mass of a single platinum atom. The additional interplanar terms which have not been given explicitly in Eqs. (17) are dominated by $\beta_1^{\perp}$, as is to be expected. To proceed further, we must also examine the nature of the normal-mode motions corresponding to these modes. Figure 23 shows the results of a displacement analysis from calculations with the modified force constants at $\bar{K}$. Since the corresponding normal-mode motions at $\bar{M}$ are even more complicated, we will concentrate on discussing the forces in terms of the modes at $\bar{K}$. To the right of each of the diagrams, the amplitudes of the polarization vector in the first three layers indicate that three modes involve a sequence of in-plane and out-of-plane motions in the successive layers, with pure vertical motions in the top layer for the PR mode and pure in-plane motions in the top layers for the R and LR modes.

Examination of Fig. 23 and Eq. (17d) indicates that the transverse PR mode at $\bar{K}$ is affected almost entirely by bending motions normal to the plane. The stiffening of the surface plane with respect to out-of-plane bending displacements is described by the increase in $\alpha_1^{\parallel}$, which, in fact, affects both in-plane and out-of-plane motions. As we shall discuss below, the effect of increasing $\alpha_1^{\parallel}$ on in-plane motions within the surface layer is largely compensated for by the changes in the other force constants $\beta_1^{\parallel}$ and $\delta_1^{\parallel}$ in the top layer [Fig. 23(b)]. From this analysis the importance of including tangential forces becomes apparent. If these had not been present in the calculation, then we would have had to change $\beta_1^{\perp}$, which has an effect on the frequencies of all the other surface modes. Thus, in one recent calculation based only on $\beta_1^{\perp}$ and $\beta_1^{\parallel}$, it was necessary to assume vibrations in the second layer in order to explain the experimentally observed resonances.[8] Such an explanation cannot be correct for He-atom scattering experiments since the modes in the second layer have only a very small direct effect on the scattering. This can be understood from the short range of the He-atom surface potential and the resulting small contributions from the second layer. Note also that the inclusion of $\alpha_1^{\parallel}$ in the first layer takes full account of the effect of surface stress in the first layer, which has to be introduced separately in a model based only on nearest-neighbor radial force constants.[75]

Next, we observe from Eq. (17) that the other constants $\beta_1^{\parallel}$ and $\delta_1^{\parallel}$ influence only the motions in the surface plane. Moreover, as can be seen from Eqs. (17c) and (17d), the observed decrease in both $\beta_1^{\parallel}$ and $\delta_1^{\parallel}$ compensate for the increase in $\alpha_1^{\parallel}$. This can be interpreted as indicating that the in-plane effect of increasing $\alpha_1^{\parallel}$ is, in fact, not of physical significance for these modes. Moreover, from Eqs. (17b) and (17c) we see that $\beta_1^{\parallel}$ and $\delta_1^{\parallel}$ operate in the same direction and their relative contributions arise, in fact, from the fit of the dispersion curves for the surface-localized modes at smaller values of the wave vector Q.

With these preliminary remarks, we can now attempt to interpret the force constants in terms of a simple model of electronic charge redistribution at the surface in the same spirit as in electronic models of surface structural

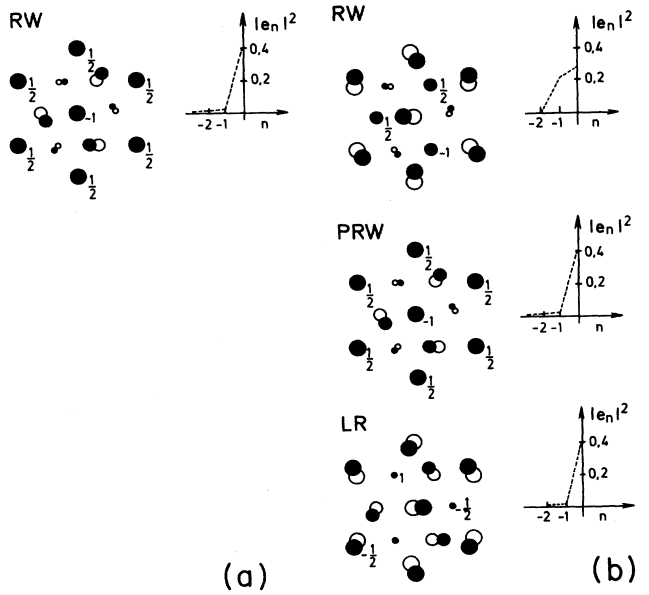

FIG. 23. The normal-mode motions for the atoms in the first three planes of the Pt surface at $\bar{K}$ are shown for the surface described by unmodified bulk force constants in (a), and for the surface described by surface modified force constants as obtained by a best fit of the data in (b). The largest circles represent atoms in the top layer, etc. The open circles are the equilibrium positions, and + and − denote motions out of the plane. The curves on the right of each diagram show the predicted decrease in amplitudes with penetration into the surface.

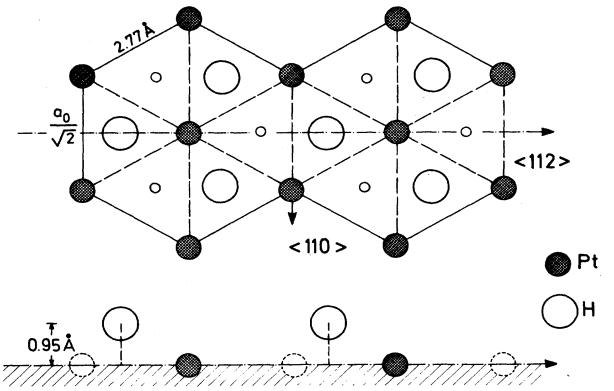

FIG. 24. A structural model of the Pt(111)+H(1×1) surface, adapted from Ref. 33. The large open circles denote the adsorbed hydrogen atoms, the shaded circles the Pt atoms of the surface plane, and the small solid circles the Pt atoms of the second layer.

relaxation. For the bulk there is considerable evidence in *d*-electron metals such as Au that there is a substantial concentration of electronic charge due to *sp-d* hybridization in the bonding region between the atoms, similar to that calculated for Si.[76] It was found[76] that the bonding charge can be described by a three-body interaction in the solid similar to the angular part of the interatomic potential that we have used in this paper. Furthermore, the effect of the bonding charge on the dynamics of the bulk crystal is to increase the frequency of the phonon modes, which corresponds to an extra repulsive force between the ions. This is in accord with the Hellman-Feynman theorem, which states that the forces on the nuclei in a quantum-mechanical system can be explained by the electrostatic interaction of ions to the electrons located between the ion cores. Thus, a reduction in $\beta_1^{\parallel}$ corresponds to a displacement of electronic charge away from the bonding region.

With respect to the surface plane, there are several pieces of evidence indicating that the electrons spill out from the surface layer in much the manner as first suggested by Smoluchowski.[42] For one, the increase of $\alpha_1^{\perp}$ which removes the small inward relaxation predicted by the bulk force constants is consistent with the Hellman-Feynman theory if there is an increase in the electronic charge density above the surface layer. The increase of $\alpha_1^{\parallel}$ also would seem to indicate a stiffening of the surface layer, which is expected if the bonding electrons are more uniformly distributed above the outermost layer of the ion cores to form a more stable "cage" distributed over the surface.

The effect of hydrogen can also be understood in terms of electron redistribution. Recall that the hydrogen atoms are thought to be located in fcc sites (see Fig. 24) at about 0.95 Å above the surface layer. From charge-density calculations for Li atoms adsorbed on a jellium surface, it is known that electropositive ions tend to lead to an increase of the electron density in the surface region below the adsorbed atom.[77] Thus, in the structure of Fig. 24 the increased electron density will tend to stiffen the bonds between the three Pt atoms at the base of the triangle. To be sure, it is surprising that this effect exactly compensates the softening produced by the spilling out of electrons. The observed additional, small outward relaxation for the hydrogen-covered surface implies also that the hydrogen atoms draw some of the electrons further away from the solid. This is consistent with the weak oscillatory electron-density changes in jellium calculations[77] of the electron-density contours in the vicinity of surface adsorbates. According to this explanation, the reduction in electronic density in the minima will tend to weaken the interplanar force constants.

Thus, in conclusion, we are able to explain all the observed effects in terms of a redistribution of electronic charge at the surface. A possible explanation for the observed charge redistribution is the reduction at the surface of the *sp-d* hybridization, which is responsible for the directed bonding charge between atoms in the bulk. We recall that a similar effect is also present in the noble metals. It is interesting to note that in these metals with a closed *d* shell the reduction of $\beta_1^{\parallel}/\beta_1^{b}$ increases from 0.50 for Ag(111) (Ref. 4) to about 0.30 in Au(111).[69] This sequence coincides with the expected increasing strength of *sp-d* hybridization in passing from 4*d* (Ag) to 5*d* (Au) closed shells. Pt, as a transition metal, has one less elec-

tron than Au and it is interesting to see that the softening of $\beta\|$ is indeed quite similar in both metals. It will be interesting to see if Ni and Pd will show the same behavior with respect to the corresponding noble metals Cu and Ag. Work on the same analysis of experimental surface-phonon dispersion curves available for Ni(100), Pd(110), and Cu(111) is in progress.

ACKNOWLEDGMENTS

We are grateful to K. M. Bohnen, V. Celli, and C. S. Jayanthi for several valuable discussions. Three of us (V.B., A.F., and G.S.) acknowledge the Computational Center (CICAIA) of the University of Modena for computing support.

[1]R. B. Doak, U. Harten, and J. P. Toennies, Phys. Rev. Lett. **51**, 578 (1983).
[2]V. Bortolani, G. Santoro, U. Harten, and J. P. Toennies, Surf. Sci. **148**, 82 (1984).
[3]U. Harten, J. P. Toennies, and Ch. Wöll, Faraday Discuss. Chem. Soc. **80**, 1 (1985).
[4]V. Bortolani, A. Franchini, F. Nizzoli, and G. Santoro, Phys. Rev. Lett. **52**, 429 (1984).
[5]C. S. Jayanthi, H. Bilz, W. Kress, and G. Benedek, Phys. Rev. Lett. **59**, 795 (1987).
[6]U. Harten, J. P. Toennies, Ch. Wöll, and G. Zhang, Phys. Rev. Lett. **55**, 2308 (1985).
[7]D. Neuhaus, F. Joo, and B. Feuerbacher, Surf. Sci. **165**, L90 (1986).
[8]K. Kern, R. David, P. L. Palmer, G. Comsa, and T. S. Rahman, Phys. Rev. B **33**, 4334 (1986).
[9]G. Lilienkamp and J. P. Toennies, J. Chem. Phys. **78**, 5210 (1983).
[10]J. P. Toennies and K. Winkelman, J. Chem. Phys. **66**, 3965 (1977).
[11]J. P. Toennies, W. Welz, and G. Wolf, J. Chem. Phys. **71**, 614 (1979); R. Götting, H. R. Mayne, and J. P. Toennies, *ibid.* **85**, 6396 (1986).
[12]B. Lantzsch (unpublished).
[13]Purchased from Goodfellow Metals, Cambridge. The purity was 99.99%.
[14]B. Poelsema, S. T. de Zwart, and G. Comsa, Phys. Rev. Lett. **49**, 578 (1982); **51**, 522 (1983).
[15]A. M. Lahee, J. R. Manson, J. P. Toennies, and Ch. Wöll, Phys. Rev. Lett. **57**, 471 (1986).
[16]G. Boato, P. Cantini, and R. Tatarek, J. Phys. F **6**, L237 (1976).
[17]J. M. Horne, S. C. Yerkes, and P. R. Miller, Surf. Sci. **93**, 47 (1980).
[18]U. Garibaldi, A. C. Levi, R. Spadacini, and G. E. Tommei, Surf. Sci. **48**, 649 (1975).
[19]J. Lee, J. P. Cowin, and L. Wharton, Surf. Sci. **130**, 1 (1983).
[20]U. Harten, J. P. Toennies, and Ch. Wöll, J. Chem. Phys. **85**, 2249 (1986).
[21]T. M. Lu and M. G. Lagally, Surf. Sci. **120**, 47 (1982).
[22]J. Lapujoulade, Surf. Sci. **108**, 526 (1981).
[23]G. Brusdeylins, R. B. Doak, and J. P. Toennies, Phys. Rev. B **27**, 3662 (1983).
[24]D. M. Smilgies and J. P. Toennies, Rev. Sci. Instrum. **59**, 2185 (1988).
[25]G. Benedek, Phys. Rev. Lett. **35**, 234 (1975).
[26]G. Benedek, G. Brusdeylins, J. P. Toennies, and R. B. Doak, Phys. Rev. B **27**, 2488 (1983).
[27]G. Benedek, G. Brusdeylins, R. B. Doak, J. G. Skofronick, and J. P. Toennies, Phys. Rev. B **28**, 2104 (1983).
[28]D. M. Dutton, B. N. Brockhouse, and A. P. Miller, Can. J. Phys. **50**, 2915 (1972).
[29]G. W. Farnell (private communication).
[30]R. E. Macfarlane, J. A. Rayne, and C. K. Jones, Phys. Lett. **18**, 91 (1965).
[31]D. Eichenauer, U. Harten, J. P. Toennies, and V. Celli, J. Chem. Phys. **86**, 3693 (1978).
[32]K. Christmann, G. Ertl, and T. Pignet, Surf. Sci. **54**, 365 (1976).
[33]K. Christmann, Z. Phys. Chem. (Neue Folge) **154**, 145 (1987), and private communication.
[34]B. J. J. Koeleman, S. T. de Zwart, A. L. Beers, B. Poelsema, and L. K. Verheij, Phys. Rev. Lett. **56**, 1152 (1986).
[35]J. A. Davies, D. P. Jackson, P. R. Narton, D. E. Posner, and W. N. Unertl, Solid State Commun. **34**, 41 (1980).
[36]P. J. Feibelmann and D. R. Hamann, Surf. Sci. **182**, 411 (1987).
[37]I. P. Batra, Surf. Sci. **148**, 1 (1984).
[38]See, for example, K. M. Ho, C. L. Fu, and B. N. Harmon, Phys. Rev. B **29**, 575 (1984).
[39]K. M. Ho and K. P. Bohnen, Europhys. Lett. **4**, 345 (1987).
[40]O. K. Andersen, Phys. Rev. B **2**, 883 (1970); M. C. Desjonquères and F. Cyrot-Lackmann, Solid State Commun. **18**, 1127 (1976); R. P. Messmer, S. K. Knudson, K. H. Johnson, J. B. Diamond, and C. Y. Young, Phys. Rev. B **13**, 1396 (1976).
[41]E. Tosatti, C. Calandra, V. Bortolani, and C. M. Bertoni, Solid State Phys. **5**, L299 (1972); C. M. Bertoni, V. Bortolani, C. Calandra, and F. Nizzoli, J. Phys. F **4**, 19 (1974); J. Phys. C **6**, 3612 (1973); C. Falter, W. Ludwig, A. A. Maradudin, M. Selmke, and W. Zierau, Phys. Rev. B **32**, 6510 (1985); C. Falter, M. Selmke, W. Ludwig, and K. Kunc, *ibid.* **32**, 6518 (1985).
[42]R. Smoluchowski, Phys. Rev. **60**, 661 (1941).
[43]M. W. Finnis and V. Heine, J. Phys. F **4**, L37 (1974).
[44]V. Heine and L. D. Marks, Surf. Sci. **165**, 66 (1986).
[45]C. Beatrice and C. Calandra, Phys. Rev. B **28**, 6130 (1983).
[46]K. M. Ho and K. P. Bohnen, Phys. Rev. Lett. **56**, 934 (1986).
[47]A. G. Eguiluz, D. A. Campbell, A. A. Maradudin, and R. F. Wallis, Phys. Rev. B **30**, 5449 (1984); A. G. Eguiluz, *ibid.* **35**, 5473 (1987).
[48]V. Bortolani, A. Franchini, and G. Santoro, in *Electronic Structure, Dynamics and Quantum Structural Properties of Condensed Matter,* edited by J. T. Devreese and P. Van Camp (Plenum, New York, 1985), p. 401.
[49]V. Bortolani, A. Franchini, and G. Santoro, in *Dynamical Phenomena at Surfaces, Interfaces, and Superlattices,* edited by F. Nizzoli, K. H. Rieder, and R. F. Willis (Springer, Berlin, 1985), p. 92.
[50]M. Born and K. Huang, *Dynamical Theory of Crystal Lattices* (Oxford University Press, Oxford, 1954); A. A. Maradudin, *Advances in Solid State Physics* (Plenum, New York, 1981).
[51]D. Castiel, L. Dobrzynski, and D. Spanjard, Surf. Sci. **59**, 252 (1976); B. C. Clark, D. C. Gazis, and R. F. Wallis, Phys. Rev.

134, A1486 (1964); P. S. Yuen and Y. P. Varshni, *ibid.* **164**, 895 (1967); R. E. Allen, G. P. Alldredge, and F. W. De Wette, Phys. Rev. B **4**, 1648 (1971); A. A. Maradudin, *Advances in Solid State Physics* (Plenum, New York, 1981); A. A. Maradudin, E. W. Montroll, G. H. Weiss, and I. P. Ipatova, Solid State Suppl. 3 (1971).

[52]A. Levi and V. Bortolani, La Rivista Nuovo Cimento **9**, 1 (1986).

[53]N. Esbjerg and J. K. Nørskov, Phys. Rev. Lett. **45**, 807 (1980).

[54]A. D. McLean and R. S. McLean, At. Data Nucl. Data Tables **26**, 197 (1981).

[55]M. Manninen, J. K. Nørskov, M. J. Puska, and C. Umrigar, Phys. Rev. B **29**, 2314 (1984).

[56]K. T. Tang and J. P. Toennies, J. Chem. Phys. **80**, 3726 (1984).

[57]V. Bortolani, A. Franchini, N. Garcia, F. Nizzoli, and G. Santoro, Phys. Rev. B **28**, 7358 (1983).

[58]V. Bortolani, V. Celli, A. Franchini, J. Idiodi, G. Santoro, K. Kern, B. Poelsema, and G. Comsa, Surf. Sci. **208**, 1 (1989).

[59]E. Zaremba, Surf. Sci. **151**, 91 (1985).

[60]B. Poelsema, R. L. Palmer, G. Mechtersheimer, and G. Comsa, Surf. Sci. **117**, 60 (1982).

[61]V. Celli, G. Benedek, U. Harten, J. P. Toennies, R. B. Doak, and V. Bortolani, Surf. Sci. **143**, L376 (1984); V. Bortolani, A. Franchini, F. Nizzoli, G. Santoro, G. Benedek, V. Celli, and N. Garcia, Solid State Commun. **12**, 1045 (1983).

[62]H. D. Meyer, Surf. Sci. **104**, 117 (1984).

[63]S. W. Lovesey, *Theory of Neutron Scattering from Condensed Matter* (Clarendon, Oxford, 1984); G. Benedek, Surf. Sci. **126**, 624 (1983).

[64]J. P. Toennies, in *Surface Phonons,* edited by W. Kress (Springer, Heidelberg, 1988).

[65]G. W. Farnell, in *Physical Acoustics,* edited by W. P. Mason and R. N. Thurston (Academic, New York, 1970), Vol. VI, p. 109; in *Acoustic Surface Waves,* edited by A. A. Oliner (Springer, Berlin, 1978), p. 13.

[66]G. I. Stegeman and F. Nizzoli, in *Surface Excitations,* edited by V. M. Agranovich and R. Loudon (Elsevier, British Vancouver, 1984), p. 195; V. Bortolani, F. Nizzoli, and G. Santoro, J. Phys. F **8**, L215 (1978).

[67]J. R. Sandercock, Solid State Commun. **26**, 547 (1978).

[68]V. Bortolani and G. Santoro, in *Electromagnetic Surface Excitations,* edited by R. F. Wallis and G. I. Stegeman (Springer, Berlin, 1986), p. 46.

[69]G. Santoro, A. Franchini, V. Bortolani, U. Harten, J. P. Toennies, and Ch. Wöll, Surf. Sci. **183**, 180 (1987).

[70]U. Harten, J. P. Toennies, and Ch. Wöll (unpublished).

[71]J. P. Toennies, in *Proceedings of the Solvay Conference on Surface Science* (Springer, Heidelberg, 1988), p. 248.

[72]P. K. Lam and M. Cohen, Phys. Rev. B **25**, 6139 (1982).

[73]V. Bortolani, A. Franchini, G. Santoro, J. P. Toennies, A. Lock, and Ch. Wöll (unpublished).

[74]A. Franchini, Ph.D. dissertation, University of Modena, 1985/86.

[75]J. E. Müller, M. Wuttig, and H. Ibach, Phys. Rev. Lett. **56**,1583 (1986).

[76]C. M. Bertoni, V. Bortolani, C. Calandra, and F. Nizzoli, J. Phys. C **6**, 3612 (1973).

[77]N. D. Lang and A. R. Williams, Phys. Rev. Lett. **37**, 212 (1976).